



HAL
open science

FTIR micro-spectroscopy using synchrotron-based and thermal source-based radiation for probing live bacteria

Julie Meneghel, Stephanie Passot, Frédéric Jamme, Stéphane Lefrançois,
Pascale Lieben, Paul Dumas, Fernanda Fonseca

► To cite this version:

Julie Meneghel, Stephanie Passot, Frédéric Jamme, Stéphane Lefrançois, Pascale Lieben, et al.. FTIR micro-spectroscopy using synchrotron-based and thermal source-based radiation for probing live bacteria. *Analytical and Bioanalytical Chemistry*, 2020, 412 (26), pp.7049-7061. 10.1007/s00216-020-02835-x . hal-03824330

HAL Id: hal-03824330

<https://hal.science/hal-03824330>

Submitted on 21 Oct 2022

HAL is a multi-disciplinary open access archive for the deposit and dissemination of scientific research documents, whether they are published or not. The documents may come from teaching and research institutions in France or abroad, or from public or private research centers.

L'archive ouverte pluridisciplinaire **HAL**, est destinée au dépôt et à la diffusion de documents scientifiques de niveau recherche, publiés ou non, émanant des établissements d'enseignement et de recherche français ou étrangers, des laboratoires publics ou privés.

FTIR micro-spectroscopy using synchrotron-based and thermal source-based radiation for probing live bacteria

Julie Meneghel^a, Stephanie Passot^a, Frederic Jamme^b, Stephane Lefrançois^b, Pascale Lieben^a, Paul Dumas^b and Fernanda Fonseca^{a*}

^a Université Paris-Saclay, INRAE, AgroParisTech, UMR SayFood, 78850, Thiverval-Grignon, France

^b Synchrotron SOLEIL, L'Orme des Merisiers, Saint Aubin, BP 489, Gif-sur-Yvette, 91192, France

*Correspondance email: fernanda.fonseca@inrae.fr

ORCID numbers:

Julie Meneghel: 0000-0002-1510-8642

Stéphanie Passot: 0000-0003-2799-5493

Frédéric Jamme: 0000-0002-7398-7868

Paul Dumas: 0000-0002-9878-8048

Fernanda Fonseca: 0000-0003-3394-182X

Abstract

Fourier transform infrared (FTIR) spectroscopy has proven to be a non-invasive tool to analyse cells without the hurdle of employing exogenous dyes or probes. Nevertheless, the study of single live bacteria in their aqueous environment has long remained a big challenge, due to the strong infrared absorption of water and the small size of bacteria compared to the micron-range infrared wavelengths of the probing photons. To record infrared spectra of bacteria in an aqueous environment, at different spatial resolutions, two setups were developed. A custom-built Attenuated Total Reflection inverted microscope was coupled to a synchrotron-based FTIR spectrometer, using a germanium hemisphere. With such a setup, a projected spot size of $1 \times 1 \mu\text{m}^2$ was achieved, which allowed spectra acquisition at the single-cell level in the $1800 - 1300 \text{ cm}^{-1}$ region. The second setup used a demountable liquid micro-chamber with a thermal-source powered FTIR microscope, in transmission geometry, for probing clusters of few thousands of live cells in the mid-IR region ($4000 - 975 \text{ cm}^{-1}$). Both setups were applied for studying two strains of a model lactic acid bacterium exhibiting different cryo-resistances.

The two approaches allowed the discrimination of both strains and revealed population heterogeneity among bacteria at different spatial resolutions. The multivariate analysis of spectra indicated that the cryo-sensitive cells presented the highest cell heterogeneity and the highest content of proteins in α -helix structure. Furthermore, the results from clusters of bacterial cells evidenced phosphate and peptidoglycan vibrational bands associated with the cell envelope, as potential markers of resistance to environmental conditions.

Keywords: lactic acid bacteria, freezing, FTIR, aqueous environment, population heterogeneity

Introduction

Fourier transform infrared (FTIR) micro-spectroscopy is a powerful analytical technique used for characterizing cells and tissues. It is a non-invasive tool since it does not require exogenous probes or contrast agents and it does not induce radiation damage to cells, even if high brightness infrared beam is used [1, 2]. The mid-IR region ($4000 - 400 \text{ cm}^{-1}$) provides a non-restrictive chemical description of the major cellular components (e.g. lipids, proteins, carbohydrates, and nucleic acids). In microbiology, it has been mainly exploited to characterize samples containing millions of cells (colonies, cell pellets, etc.) and it has largely proved to be efficient for identifying micro-organisms [3–6] and for assessing molecular changes of food-associated micro-organisms in response to stress conditions [7–9].

Many industrial processes involve bacteria (e.g. the production and preservation of bacteria used as starters in fermented foods, or the inactivation of foodborne pathogens). Analysing the biochemical composition of bacteria appears crucial for identifying molecular biomarkers of bacterial resistance to environmental conditions, and thus for improving process efficiency. Furthermore, probing bacteria at the single-cell level could reveal bacterial population heterogeneity and could enable – by reverse-engineering – the identification of appropriate processing conditions for recovering homogeneous bacterial populations with target functionalities (e.g. metabolites production or health properties). Due to the very small dimension of single bacterial cells (approximately ten times smaller than eukaryotic cells), the use of a brighter source than the one traditionally used (thermal source) is mandatory. Synchrotron radiation-based Fourier transform infrared (SR-FTIR) micro-spectroscopy has indeed been successfully applied to study bacteria at the single-cell level in a dry state [10, 11]. This allowed the study of bacterial biochemical modifications after exposure to stressful conditions and population heterogeneity. However, the biochemical characterization of individual live bacterial cells by FTIR spectroscopy in aqueous environments remains a challenge.

In FTIR micro-spectroscopy, the presence of water is the main obstacle due to its strong infrared absorbance in the same mid-IR frequency region as major biological components. Water absorption bands at $3500 - 3000 \text{ cm}^{-1}$ (O-H stretching mode) and at approximately 1650 cm^{-1} (O-H bending mode) indeed overlap interesting spectral features arising from cell lipids and proteins, respectively. To overcome this water issue, dehydration, chemical fixation, or replacing water by deuterated water are the techniques currently employed. These techniques of sample preparation can, however, affect different cellular structures [12–14] and bacterial growth [15], limiting the interpretation of the obtained spectra.

Methods to minimize the contribution of water in IR spectra have been developed for studying live cells in aqueous solution. In transmission mode, sample devices with path lengths lower than $10 \mu\text{m}$ were used to reduce the beam path through the water layer. For example, an open-channel microfluidic device was developed for the analysis of microbial biofilms [16]. Demountable liquid cells [17], closed-channel microfluidic devices [18, 19] have also been used to study micron-sized single eukaryotic cells (at approximately $10 \mu\text{m}$ spatial resolution) in aqueous environments. In these studies, the high spatial resolution provided by synchrotron radiation (SR) through its intrinsic photon flux density, has allowed biochemical mapping at the sub-cellular level. Recently, Chan et al. [20, 21] developed a transmission liquid cell composed of two ZnSe hemispherical lenses tightly closed employing a screw ring and a thin spacer of $6 \mu\text{m}$ controlling the path length. This new device was first tested using synchrotron FTIR microscopy for studying live cells at a lateral resolution close to $2.2 \mu\text{m}$ at $6 \mu\text{m}$ wavelength [20]. Then,

Chan et al. [21] extended the application of this transmission device to FPA imaging and linear array imaging systems. However, performing experiments in transmission mode required the correction of the protein-related bands (in particular the amide I band) to remove the strong contribution of the water bending modes. Semi-automatic water subtraction procedures were suggested [18, 22] to eliminate operator subjectivity and processing large numbers of spectra.

In parallel, ATR configurations have been used to study adherent live cells. The direct growth of bacterial biofilms onto ATR crystals enabled the infrared analysis of adherent bacteria [23–27]. In such a configuration, a liquid medium flows over the biofilm and the evanescent wave produced interacts with bacterial cells in intimate contact with the ATR crystal. Moreover, Kuimova et al. [27] pioneered in combining ATR hemisphere with FTIR micro-spectroscopy to map seeded adherent eukaryotic cells in solution. Cells and the solution were maintained by capillary forces on the surface of removable ATR hemispheres and analysed with 4 μm of estimated spatial resolution [28]. Regardless of the FTIR micro-spectroscopy device, the investigation of live prokaryotic cells, being approximately ten times smaller than eukaryotic cells, is today limited to the study of clusters of millions of adherent cells.

Our research activities focus on industrial processes for producing frozen and freeze-dried concentrates of lactic acid bacteria. The improvement of bacterial viability and process efficiency requires the identification of cellular components involved in bacterial resistance and the capability of producing homogenous cell populations. FTIR spectroscopy appears as a relevant tool for screening bacterial strains and defining optimal process operating conditions. Previously, we investigated lactic acid bacteria in the dried state at the single-cell level by combining synchrotron infrared and fluorescence microscopy and evidenced population heterogeneity [10]. In the present study, our objective was to develop FTIR micro-spectroscopy devices for probing live bacteria and to compare the biochemical data obtained at the single-cell level with data obtained from clusters of thousands of cells using a bench-top instrument. In particular, evaluating the possibility of evidencing bacterial population heterogeneity by analysing clusters of cells was also undertaken.

To address the challenge of biochemical characterization of single-cell bacteria in an aqueous environment, we developed a dedicated setup consisting of an ATR-FTIR inverted microscope, which was coupled to the synchrotron radiation of the SMIS beamline of SOLEIL facility. At the bench-top level, a custom-made transmission demountable cell was coupled to an FTIR microscope with a thermal source. More particularly, we have studied *Lactobacillus delbrueckii* subsp. *bulgaricus* (*L. bulgaricus*) in an aqueous environment. *L. bulgaricus* is a lactic acid bacterium (rod-shaped of about 3-6 μm length and 1 μm diameter), widely used as a starter for manufacturing cheese, fermented milk, meat, vegetables, bread and healthcare products, and exhibiting variable resistance to freezing. After the acquisition, the infrared spectra were processed to remove the spectral contribution of water using a program developed on purpose. In this article, we present the first results obtained with both devices on the biochemical characterization of two *L. bulgaricus* strains in an aqueous environment. The secondary structure of proteins and components of the cell envelope were proposed as potential markers of cryo-resistance.

Methods

Bacterial samples – cultivation conditions and preparation of cell suspensions

Two strains of the lactic acid bacterium *Lactobacillus delbrueckii* subsp. *bulgaricus* were used in this study: CFL1 (CIRM-BIA; Rennes, France) and ATCC 11842 (Manassas, VA, USA). They were cultivated according to the procedure described by Meneghel et al. [29], resulting in the recovery of cryo-sensitive *L. bulgaricus* CFL1 and cryo-resistant *L. bulgaricus* ATCC 11842 bacterial populations.

Upon harvest, cells were washed twice with Tris-HCl buffer (50 mM, pH 8.8, Bio-Rad; Hercules, CA, USA) to remove growth residues and metabolites that may contribute to the vibrational spectra. Cells were additionally washed in saline solution and re-suspended in a 1:1 (wt:wt) ratio of a saline solution before analysis.

Synchrotron radiation-based ATR-FTIR inverted microscope

The development of an ATR-FTIR inverted microscope and the associated experiments were carried out in collaboration with the beamline scientists at the SMIS beamline of the SOLEIL synchrotron facility (Saint-Aubin, France). The device was adapted from the configuration used by Saulou et al. [11] and Passot et al. [10] for analysing spectra of individual dried bacterial cell (Fig. 1a) and the configuration described by Kuimova et al. [27] and then by Kazarian and Chan [28] for analysing adherent live cells in intimate contact with the ATR hemisphere (Fig. 1b). This configuration was turned over in the present work (Fig. 1c) to easily introduce samples directly on the surface of a high refractive index hemisphere and to make the analysis of a solution of non-adherent cells possible.

Figure 2 shows a picture of the ATR-FTIR inverted configuration (Fig. 2a) as well as, a schematic overview of the device with the optical path of the infrared beam (Fig. 2b), and enlargements of the system including the IR objective, ATR hemisphere and sample chamber (Fig. 2c) and the ATR hemisphere with a bacterial deposit on its surface (Fig. 2d). The synchrotron source, coupled to the FTIR spectrometer, is directed outwards towards the inverted microscope, and an intermediate image is created using a pair of parabolic mirrors, to set an adjustable aperture at this image stage. A 45° tilted mirror is installed before the focusing objective (Schwarzschild, 32×, NA = 0.65) to mask half of the incoming beam, and collect the returned beam, for directing it to an MCT (mercury cadmium telluride) infrared detector (Thermo Fischer Scientific). We used a germanium (Ge) hemisphere (refractive index $RI_{Ge} \approx 4.01$ in the mid-IR region) as the ATR component. With an intermediate aperture of 128 x 128 μm^2 size, accounting for the x32 enhancement of the Schwarzschild and the Ge refractive index, we estimate that the projected spot size on the sample is approximately 1 x 1 μm^2 .

The flat face of the Ge hemisphere constituted the base of the liquid sampling chamber, as shown in Fig. 2c. The body of the chamber was appended to the base of the ATR hemisphere with a circular seal in between and water-tightness was guaranteed by pressing the assembly together thanks to a rotating ring (Fig. 2b). The liquid chamber was closed with a screw cap to avoid water evaporation during experiments. Hemisphere and liquid chamber were supported by an X Y linear translation stage (Prior stage, 0.1 μm precision). The whole was enclosed in a box made in Plexiglas® that was purged with dry air.

At the interface between Ge hemisphere and medium containing bacteria, an evanescent wave is created and penetrates the sample, to a depth (d_p) depending on the wavelength λ , according to the following equation:

$$dp = \frac{\lambda}{2 \pi RI_{Ge}} \sqrt{\sin^2 \alpha - \left(\frac{RI_{Ge}}{RI_{sample}} \right)^2}$$

where RI_{Ge} and RI_{sample} are the refractive indexes of the Ge ATR crystal (4.01) and sample (considered similar to water, 1.5), respectively, and α is the angle of incidence (30° in our configuration). Under such conditions, the penetration depth (d_p) of the evanescent wave was shallower than $1.6 \mu\text{m}$ (d_p at 3000 cm^{-1} (lipid region) = $0.53 \mu\text{m}$; at 1650 cm^{-1} (proteins region) = $0.96 \mu\text{m}$; and at 1000 cm^{-1} (carbohydrates region) = $1.59 \mu\text{m}$). In such a configuration, and given the size of the rod-shaped bacteria under investigation ($1 \mu\text{m}$ thick x $3 - 6 \mu\text{m}$ long) as determined in a previous study [29], the absorption of IR light essentially arose from portions of one or two bacteria plus some surrounding and underlying water.

All spectra were recorded with the Omnic software (Version 8.1, Thermo Scientific, USA). A background spectrum was acquired (128 co-added scans, 4 cm^{-1} resolution) without any sample on the surface of Ge hemisphere. Then, a volume of $10 \mu\text{L}$ of saline solution (the diluent) was deposited in the chamber and a second spectrum was acquired. Saline water was then removed, and dryness of the hemisphere was verified by checking the disappearance of the water O-H stretching vibration (the broad band centred at $\sim 3400 \text{ cm}^{-1}$) in the preview mode of the Omnic software. A volume of $10 \mu\text{L}$ of a bacterial suspension in saline solution was then deposited in the chamber. Spectral features of bacterial cells appeared gradually as cells settled down in contact with the hemisphere. The $5 \mu\text{m}$ translation step of the X Y stage ensured to probe different cells at each position (projected beam size: $1 \times 1 \mu\text{m}^2$) within a sampling area of typically of $60 \times 60 \mu\text{m}^2$, centred at the hemisphere's centre point. A total of approximately 100 spectra were recorded (128 co-added scans, 4 cm^{-1} resolution) per sample deposit.

Thermal source transmission FTIR microscope

The thermal source transmission FTIR experiments were carried out using a Nicolet IN10 infrared microscope (Thermo Scientific, USA) with a permanently aligned objective ($15\times$, $NA = 0.7$), hereafter referred to as "transmission FTIR microscope". A specific demountable sample holder for liquid samples was designed (Fig. 3a-b) fitting a CaF_2 micro-chamber (Hellma Analytics, Paris, France) which could be maintained tightly closed (Fig. 3c).

A thin strip of Mylar (polyethylene terephthalate film of $2.5 \mu\text{m}$ thickness from GoodFellow, Lille, France) was placed in the middle of the CaF_2 chamber to separate it into two parts (Fig. 3d). One μL of saline water (the diluent) was deposited over one side of the disc and $1 \mu\text{L}$ of bacterial suspension over the other side. The lid was immediately appended to avoid sample drying and the chamber was maintained tightly closed in the dedicated sample holder which was placed on the transmission FTIR microscope. Chamber height (path length) was accurately determined by counting the complete peak to peak interferences fringes appearing on spectra ($4.3 \mu\text{m} \pm 0.7 \mu\text{m}$ = mean of 8 measurements after mounting and dismounting the custom-made sample holder containing the CaF_2 micro-chamber). All spectra were recorded with the Omnic software. A background spectrum was recorded in an air bubble in the diluent region and spectra were recorded at different positions in the diluent and bacterial locations (128 co-added scans, 8 cm^{-1} resolution). Aperture was set at $50 \times 50 \mu\text{m}^2$, making a sampled volume of approximately $10^4 \mu\text{m}^3$. The approximate volume of *L. bulgaricus* cells being a few μm^3 (about $6 \mu\text{m}^3$ for *L. bulgaricus* CFL1 and about $3 \mu\text{m}^3$ for *L. bulgaricus* ATCC 11842) [30], the estimated number of probed

bacterial cells with this experimental setup could, therefore, be roughly estimated at a few thousands. Sample drying was never observed following chamber dismounting.

Spectral processing / Data processing and analysis

Pre-processing of raw spectra

The Omnic software was used for spectral sorting – to remove spectra displaying Mie scattering or Mylar absorption features – and an automatic atmospheric correction was applied to remove the residual contribution from water vapour and carbon dioxide to all spectra (ATR and transmission configuration, bacteria and diluent spectra). The advanced ATR correction tool from Omnic was additionally applied to the spectra for considering the wavelength-dependent penetration depth of the IR radiation, with the following parameters: $RI_{Ge} = 4.01$, sample $RI = 1.5$, angle of incidence = 30° , number of bounces = 1. In total, 549 spectra were recorded with the ATR configuration at the single-cell level and kept for analysis (282 for *L. bulgaricus* CFL1 and 267 for *L. bulgaricus* ATCC 11842), and 406 with the transmission configuration (225 for *L. bulgaricus* CFL1 and 181 for *L. bulgaricus* ATCC 11842).

Procedure of water subtraction

The removal of bulk water contributions from live bacteria spectra was performed using an in-house Matlab script (version: 8.3.0.532, Mathworks, Natick, MA, USA) that was guided by the method developed by Vaccari et al. [18]. To calibrate our water subtraction program, we used the value of the amide I/II area ratio determined on dried bacterial samples. According to our experience on dried bacteria [10], the amide I/II area ratio, calculated from infrared spectra of single-cell bacteria dried on the surface of ATR-hemisphere acquired using synchrotron radiation, is a constant parameter within a bacterial population.

Our script involves removing a scaled diluent spectrum to the spectra of live bacteria, with the scaling factor determined by an algorithm designed to optimize the amide I/II area ratio. The water subtraction procedure was applied to spectra obtained with both the ATR and the transmission configurations.

The reference value of the amide I/II area ratio of the two strains of *L. bulgaricus* (CFL1 and ATCC 11842) was defined from ATR-FTIR spectra of dried bacterial cells recorded on Ge hemispheres. The calculation of the area ratio was performed on pre-processed spectra between 1727 cm^{-1} and 1584 cm^{-1} (amide I), and between 1584 cm^{-1} and 1481 cm^{-1} (amide II), respectively, with a baseline extending from 1727 cm^{-1} to 1481 cm^{-1} . The amide I/II area ratios for both strains in the dry state were: 2.17 for *L. bulgaricus* CFL1 and 2.34 for *L. bulgaricus* ATCC 11842.

In Fig. 4 is presented the pre-processed spectrum recorded on a cluster of few thousands of live bacterial cells (Fig. 4a), the corresponding diluent (saline water) spectrum (Fig. 4b), and the best result (spectrum) of the live bacterial cell after water subtraction (Fig. 4c). For that, the spectrum in Fig.4c was obtained by running the in-house subtraction procedure with a range of scaling factors (from 0.6 to 1 with a step of 0.02) (see Electronic Supplementary Material (ESM) Fig. S1).

To improve both repeatability and reproducibility of the water subtraction procedure, and for minimizing the influence of the operator bias, the Matlab algorithm automatically optimizes the value of the scaling factor [18]. An example of uncorrected and corrected spectra of live bacteria obtained in the ATR and transmission configurations is presented in Fig. 5. The removal of water contribution to the spectra was noticeable through i)

the drastic reduction of the broad and intense O-H stretching vibration band around 3400 cm^{-1} , ii) the removal of the H-O-H bending, and libration combination band spanning from approx. 2500 to 1900 cm^{-1} , as evidenced by the flat baseline produced by the subtraction procedure in this region [31], and iii) the recovery of the particular shape of the amide I and II bands ($1500 - 1700\text{ cm}^{-1}$).

Post-processing of spectra (statistical analysis)

Post-processing of water-subtracted spectra was performed with the Unscrambler® X software package (Version 10.2, CAMO Software AS, Oslo, Norway). Three spectral regions, mainly containing information about lipids ($3016 - 2800\text{ cm}^{-1}$), proteins ($1800 - 1300\text{ cm}^{-1}$), and carbohydrates plus phosphorylated molecules ($1363 - 975\text{ cm}^{-1}$) were analysed. The extended multiplicative scatter correction (EMSC) was used to normalize and correct the baseline of spectra in each of the spectral regions of interest. The spectra were additionally smoothed (Savitzky-Golay algorithm (3rd order)) with a 9-point smoothing factor when considering the $1800 - 1300\text{ cm}^{-1}$ region, and with a 5-point smoothing factor otherwise. To resolve protein secondary structures or identify precise peak locations, the second-order derivatives of FTIR spectra were calculated using a 7-points Savitzky-Golay algorithm (3rd order).

After post-processing, the data was statistically analysed by principal component analysis (PCA) to study the unsupervised variation pattern in the data using the Unscrambler® X software package. The assignment of the principal absorption bands was performed using data from the literature on bacteria (see ESM Table S1). For the sake of clarity, only relevant scores and loading plots are presented in the Results and discussion section.

Results and discussion

Analytical capabilities of the two FTIR devices developed to probe live bacteria:

Single cells and clusters of thousands of cells in an aqueous environment were characterized by the synchrotron radiation-based ATR-FTIR inverted microscope and the thermal source transmission FTIR microscope, respectively. Figure 5b displays examples of infrared spectra obtained after the water subtraction procedure for both devices. With the synchrotron radiation-based ATR-FTIR inverted microscope (black curve in Fig. 5b), two spectral regions could not be accurately exploited (red boxes in Fig. 5b): i) the 1300-900 cm^{-1} region characterizing phosphate groups, polysaccharides, and nucleic acids, and ii) the 3000-2800 cm^{-1} region characterizing fatty acids of the bacterial cytoplasmic membrane. These issues are ascribed to the strong absorption arising from the protective layers of alumina mirrors of the beamline (1300-1150 cm^{-1}) and to the limited penetration depth of the evanescent wave (approximately 0.53 μm at 3000 cm^{-1}), respectively. Considering this low value of penetration depth and the likely presence of some water between the hemisphere and the cell surface, only the external cellular components of lactic acid bacteria were probed by the evanescent wave. The external cellular components of lactic acid bacteria are the constituents of the cell wall, such as exopolysaccharides, wall peptidoglycan, teichoic acids, and proteins [32–34]. Fatty acids are part of the membrane lipid bilayer, located one layer deeper than the cell wall. The evanescent wave could only shallowly reach such lipid membrane components, thus explaining the absence of exploitable fatty acid spectral features in the single-cell analysis. Since the fatty acid membrane composition can play a role in the bacterial response to environmental stress, the transmission FTIR microscope set up offers advantages over the synchrotron radiation-based ATR-FTIR inverted microscope to exploit information of the lipid bands.

The two developed FTIR devices allowed the biochemical characterization of the bacterial populations in the 1800-1300 cm^{-1} spectral region (green box in Fig. 5b). With the synchrotron radiation-based ATR-FTIR inverted microscope, the penetration depth of the evanescent wave in this spectral region was approximately 1 μm . It can thus be estimated that at least half of the thickness of a bacterial cell was probed by the infrared beam. In the case of the thermal source transmission FTIR microscope, several layers (around 4 layers) of bacterial cells contributed to the infrared spectra.

Characterization of two L. bulgaricus strains by ATR and transmission FTIR configurations in the 1800 – 1300 cm^{-1} spectral region

The feasibility of the two developed FTIR devices to probe live bacteria was demonstrated, in particular in the 1800 – 1300 cm^{-1} spectral region. An additional objective of our work was to evaluate the efficiency of the bench-top device compared to the single-cell analysis allowed by the synchrotron-based ATR-FTIR inverted microscope to access bacterial population heterogeneity. Principal component analyses were performed both using the two sets of data obtained with the ATR-FTIR inverted microscope and the transmission FTIR microscope separately (see ESM Fig. S2 and Fig. S3), and combined (Fig. 6 and see ESM Fig. S4 and Table S2). PCA were performed on normalized and smoothed water-subtracted spectra. Table S2 summarizes and compares the results obtained from the three PCA. Regardless of the dataset considered, the analysis discriminated the bacterial strains according to similar spectral features. As expected, probing live cells at the single-cell level using the synchrotron-based ATR-FTIR inverted microscope evidenced a higher level of heterogeneity within the bacterial population than probing clusters of thousands of cells (see ESM Fig. S2, Fig. S3).

When combining the two datasets in the PCA, the three first principal components (PC) explained more than 90 % of the variance of the spectral dataset. The results concerning PC1 (variability 52 %) and PC2 (variability 36 %) are displayed in Fig. 6a, 6b, and 6c, whereas the contribution of PC3 (variability 5 %) to the analysis is presented in ESM Fig. S4. The spectra acquired using the transmission FTIR configuration are represented with full symbols (Fig. 6a) and appeared included within the spectra acquired using the inverted ATR-FTIR configuration, represented with open symbols, regardless of the strain considered (in purple for the cryo-resistant strain ATCC 11842 and pink for the cryo-sensitive strain CFL1).

The PCA score plots showed a cluster separation according to the *L. bulgaricus* strain, using the second and the third principal components (PC2 and PC3) (Fig. 6a and Fig. S4b in ESM), whereas PC1 appeared related to the dispersion within the bacterial spectra of a given strain (Fig. 6a). The population of *L. bulgaricus* CFL1 cells are mainly located in the negative area of PC2 from positive to negative directions of PC3 (Fig. S4b in ESM). Two subpopulations of *L. bulgaricus* ATCC 11842 appeared located in the positive direction of PC2 and the negative direction of PC3.

The loading plots of PC2 and PC3 (Fig. 6b and Fig. S4c) revealed that major contribution to the spectral differences between the two strains arose from spectral characteristics of the amide I ($1700 - 1600 \text{ cm}^{-1}$) band, probably overlapping with nucleic acid weak features ($1715 - 1680 \text{ cm}^{-1}$), and the amide II ($1550 - 1500 \text{ cm}^{-1}$) band, *i.e.* from the protein components of cells. Positive peaks in the loading plot of PC2 (and negative peaks in the loading plot of PC3) correspond to spectral features mainly associated with the cells of *L. bulgaricus* ATCC 11842.

To further analyse the secondary structure of proteins, the second derivative of one individual spectrum of each strain, obtained using the ATR-FTIR inverted microscope (Fig. 6d) was plotted (purple and pink arrows in the score plot, Fig. 6a). The second derivatives of spectra acquired using the transmission FTIR microscope for both strains are displayed in ESM Fig. S5b. Cells of *L. bulgaricus* CFL1 (cryo-sensitive cells) appeared to be specifically characterized by a higher content of α -helix protein secondary structures ($1657 - 1655 \text{ cm}^{-1}$) than the cells of *L. bulgaricus* ATCC 11842 (cryo-resistant cells), which in turn seemed to be characterized by a higher content of pleated β -sheets and β -turns protein structures ($1685 - 1680 \text{ cm}^{-1}$) than the cryo-sensitive cells. Variations in the β -sheet bands' positions ($1685 - 1680 \text{ cm}^{-1}$ and $1640 - 1630 \text{ cm}^{-1}$, Fig. 6d) between both strains may be associated with different numbers of strands, lower wavenumbers being indicative of a higher number of strands [35].

Depending on the bacterial strain and on the environmental growth conditions (e.g. medium composition, temperature, pH, growth time), bacteria express differently their genome and could synthesize specific proteins [36–39]. By probing dehydrated *L. bulgaricus* CFL1 cells with SR-based ATR microscope, α -helix protein secondary structure (1656 cm^{-1}) characterized cells grown in MRS medium while β -pleated sheet secondary structure ($1631 - 1627 \text{ cm}^{-1}$) was associated with growth in whey medium [10]. Our present data shows differences in the protein secondary structure for two strains, *L. bulgaricus* CFL1 and ATCC 11842, grown in the same culture medium (whey) and analysed in an aqueous environment. Such differences in protein structure are certainly due to distinct genome expressions for protein synthesis and they could be related to bacterial cryo-resistance.

When considering the loading plot of PC1 (Fig. 6c), dispersion within the bacterial population appeared to be associated with the amide I protein spectral features, in particular with antiparallel pleated sheets and β -turns ($1720 - 1675 \text{ cm}^{-1}$), and β -pleated sheet ($1640 - 1600 \text{ cm}^{-1}$) protein secondary structures. The cryo-sensitive bacterial

population of *L. bulgaricus* CFL1 appeared more heterogeneous than the cryo-resistant one (*L. bulgaricus* ATCC 11842), regardless of the FTIR device. Nevertheless, the synchrotron-based ATR-FTIR inverted microscope (open symbols in Fig. 6a) enables a better estimation of population heterogeneity than the transmission FTIR microscope (full symbols in Fig. 6a). To further analyse the sample heterogeneity noticed in Fig. 6a, we show in Fig. 6e the second derivatives of the infrared spectra of the two most distant points along the PC1 axis of the PC1-PC2 score plot (grey arrows in Fig. 6a). Each selected point corresponds to the spectrum of a single cell of *L. bulgaricus* CFL1. The second derivatives of the spectra of the two most distant points for clusters of thousands of cells of *L. bulgaricus* CFL1 are displayed in ESM Fig. 5c. The heterogeneity of *L. bulgaricus* CFL1 population could be ascribed to protein secondary structures, in particular to the proportion between α -helix (1655 cm^{-1}) and β -sheet (1637 cm^{-1}) protein secondary structures.

Having access to cell-to-cell variations enables the understanding of the microbiological processes and physiological mechanisms that can be masked by measurements in bulk samples [40–42]. Moreover, the evaluation of population heterogeneity is relevant to different applications. For example, it allows the screening of microorganisms or for a given one, controlling production processes and detecting deviations (e.g. not obtaining the desired bacterial physiological state associated with a target functionality). Furthermore, relating single-cell biochemical information to the cell's physiological state can also help a reverse engineering strategy to define the experimental conditions (strains, cultivation, and cryopreservation conditions) leading to the production of homogeneous cryo-resistant populations of bacterial cells for industrial use [10, 43].

The transmission FTIR microscope enabled the discrimination of the two bacterial strains and the detection of population heterogeneity. In addition, other spectral regions than the protein one could be investigated using this configuration: the amide III and cell wall/polysaccharides ($1300 - 975\text{ cm}^{-1}$) and the lipid ($2800 - 3000\text{ cm}^{-1}$) spectral regions. Since no relevant information could be extracted from the analysis of the lipid spectral region, only the region between 1300 and 975 cm^{-1} is presented thereafter.

Characterization of the *L. bulgaricus* strains by transmission FTIR configuration in the $1300 - 975\text{ cm}^{-1}$ spectral region

Due to the strong absorption arising from the protective layers of alumina mirrors present in the synchrotron-based ATR inverted microscope in the $1300 - 1150\text{ cm}^{-1}$ region (Fig. 5b), the spectra obtained using this device could not be exploited in this region and were not included in the PCA.

PCA was performed on normalized and smoothed water-subtracted spectra acquired using the transmission FTIR microscope, in the $1360 - 975\text{ cm}^{-1}$ range. The PC1 versus PC2 score plot and the loading plots of PC1 and PC2 are reported in Fig. 7 (see PC 3 contribution in ESM Fig. S6). The PCA clustered both strains according to PC1 (76 % of total variance). To assess specific spectral features explaining the discrimination between both *L. bulgaricus* strains, we studied the loading plot of PC1 (Fig. 7b). *L. bulgaricus* ATCC 11842 (cryo-resistant) appeared to be characterized by a higher content of protein amide III band components ($1285 - 1255\text{ cm}^{-1}$) than *L. bulgaricus* CFL1 (cryo-sensitive) (Fig 7b). When considering the average spectra calculated for the two strains (Fig. 7d), large spectral differences were observed in the amide III protein region ($1310 - 1240\text{ cm}^{-1}$). The differences in the amide III region support the hypothesis of proteins implication in the cellular mechanisms of cryo-resistance previously proposed from the analysis of the amide I and amide II spectral regions. The loading plot of PC1 also indicates that the spectra of *L. bulgaricus* CFL1 cells (cryo-sensitive strain) were characterized

by a higher contribution of complex sugar ring modes ($1076 - 1052 \text{ cm}^{-1}$) from the peptidoglycan of the bacterial cell wall [44], and of PO_2^- groups ($1222 - 1200 \text{ cm}^{-1}$), than the ones of the cryo-resistant strain (Fig. 7b).

PCA also revealed a higher sample dispersion within the population of cryo-sensitive *L. bulgaricus* CFL1 (represented in pink) than the spectra of the cryo-resistant *L. bulgaricus* ATCC 11842 (represented in purple) according to PC2 (11 % of total variance) (Fig. 7a). The heterogeneity within *L. bulgaricus* CFL1 population appeared to be associated to the following spectral features: the symmetric ($1085 - 1074 \text{ cm}^{-1}$) and asymmetric ($1240 - 1210 \text{ cm}^{-1}$) stretching vibrations from PO_2^- groups, and the vibrations of the complex sugar rings modes arising from the peptidoglycan of the bacterial cell wall ($1045 - 1010 \text{ cm}^{-1}$). PO_2^- groups are involved in several cellular components: i) the phosphodiester functional groups of DNA/RNA polysaccharides backbone, ii) the polar head groups of phospholipids, and iii) phosphorus-containing carbohydrates such as teichoic acids and lipoteichoic acids (charged polymers present in the cell wall of Gram-positive bacteria). The peptidoglycan of Gram-positive bacterial wall is a multilayered polymer of sugar rings and amino acids which surrounds the cell as a protecting network and accounts for up to 60 % of the cell wall weight [44]. The cell wall-related bands have been proposed as markers of bacterial populations [10, 45, 46]. Our results from the spectral region between 1300 and 975 cm^{-1} agree with these previous studies. They also suggest that the sugar rings of peptidoglycan, the phosphate groups, as well as the amide III protein band are potential markers of cryo-resistance/cryo-sensitivity.

Conclusions

In summary, the present work showcases the first results from live lactic acid bacteria measurements with two infrared microscopy approaches. The ATR-FTIR inverted microscope developed in this work, associated with synchrotron radiation provides a way to precisely investigate cell-to-cell spectral differences. In particular, it enabled the analysis of the $1800 - 1300 \text{ cm}^{-1}$ spectral region, and thus protein secondary structures arising from one to two bacteria in aqueous solution (*i.e.*, under fully native conditions and without disturbing cellular processes). The cryo-sensitive *L. bulgaricus* CFL1 population was identified as more heterogeneous than the cryo-resistant *L. bulgaricus* ATCC 11842 population in the culture conditions studied.

On the other hand, the transmission FTIR microscope coupled with a sample holder for liquid samples also appeared as an interesting approach for the analysis of live cells in an aqueous environment, in the whole mid-IR region, by enabling the reduction and control of the optical path length. It provided intermediate access to population heterogeneity between traditional bulk FTIR spectroscopy (which likely probes 10^{5-6} cells) and single-cell resolution analysis.

From both FTIR approaches, we were able to identify some potential cellular markers of bacterial populations: secondary structure of proteins, in particular the proportions of α -helix and β -sheet structures, and cell envelope components, with more specifically polar head groups of membrane phospholipids and complex sugars of the peptidoglycan cell wall. These cellular components, already used for microbial identification purposes, seemed also to be involved in cryo-resistance mechanisms. Nevertheless, the actual involvement of these cellular components in bacterial cryo-resistance deserves to be confirmed experimentally and this hypothesis does not exclude that factors related to cryo-resistance may not be observed by FTIR spectroscopy.

Using a thermal source FTIR microscope appeared promising for preliminary or explorative works, before moving to higher spectral resolution using the bright source of the synchrotron radiation. Defining appropriate production

parameters leading to homogeneous populations of resistant cells may be an interesting outcome of this work. Coupling with microfluidic devices may also be the next step of the development to monitor evolving, dynamic processes.

Declarations

Acknowledgments and Funding Information

This work was supported by the French National Research Institute for Agriculture, Food and the Environment, (INRAE) and the French National Research Agency (ANR) under the Investing in the Future Program, Grant no. ANR-10-IDEX-0003-02. It was performed at the French national synchrotron facility SOLEIL (Gif sur Yvette, France) at the SMIS beamline (proposals no 201408998 and 20150220). We are grateful to the beamline staff for their cooperative involvement in designing and implementing the new experimental device, and for providing assistance during the experimental work and for data treatment.

Compliance with ethical standards

Conflict of interest: There are no conflict of interest to declare

Authors' contributions

JM, SP, FF and PD conceived the experimental procedure, JM, SP and FF determine the best samples to be studied, SL and PD designed and constructed the setups, JM, SP, PL and FF conducted the experiments, FJ developed an in-house Matlab script for water subtraction, JM, SP, FF analysed the data, JM, SP, FF contributed to the thorough interpretation and manuscript writing and JM, SP, FJ, FF and PD provided the critical assessment of the scientific content.

Consent for publication

All authors had full access to the data and approved the manuscript before submission

References

1. Holman H-YN, Martin MC, McKinney WR (2003) Synchrotron-Based FTIR Spectromicroscopy: Cytotoxicity and Heating Considerations. *J Biol Phys* 29:275–286
2. Miller LM, Dumas P (2010) From structure to cellular mechanism with infrared microspectroscopy. *Curr Opin Struct Biol* 20:649–656. <https://doi.org/10.1016/j.sbi.2010.07.007>
3. AlRabiah H, Correa E, Upton M, Goodacre R (2013) High-throughput phenotyping of uropathogenic *E. coli* isolates with Fourier transform infrared spectroscopy. *Analyst* 138:1363. <https://doi.org/10.1039/c3an36517d>
4. Winder CL, Goodacre R (2004) Comparison of diffuse-reflectance absorbance and attenuated total reflectance FT-IR for the discrimination of bacteria. *Analyst* 129:1118. <https://doi.org/10.1039/b408169b>
5. Udelhoven T, Naumann D, Schmitt J (2000) Development of a Hierarchical Classification System with Artificial Neural Networks and FT-IR Spectra for the Identification of Bacteria. *Appl Spectrosc* 54:1471–1479. <https://doi.org/10.1366/0003702001948619>
6. Naumann D (2006) Infrared Spectroscopy in Microbiology. In: *Encyclopedia of Analytical Chemistry*. John Wiley & Sons, Ltd
7. Alvarez-Ordóñez A, Mouwen DJM, López M, Prieto M (2011) Fourier transform infrared spectroscopy as a tool to characterize molecular composition and stress response in foodborne pathogenic bacteria. *J Microbiol Methods* 84:369–378. <https://doi.org/10.1016/j.mimet.2011.01.009>
8. Saulou C, Jamme F, Maranges C, Fourquaux I, Despax B, Raynaud P, Dumas P, Mercier-Bonin M (2010) Synchrotron FTIR microspectroscopy of the yeast *Saccharomyces cerevisiae* after exposure to plasma-deposited nanosilver-containing coating. *Anal Bioanal Chem* 396:1441–1450. <https://doi.org/10.1007/s00216-009-3316-5>
9. Lu X, Liu Q, Wu D, Al-Qadiri HM, Al-Alami NI, Kang D-H, Shin J-H, Tang J, Jabal JMF, Aston ED, Rasco BA (2011) Using of infrared spectroscopy to study the survival and injury of *Escherichia coli* O157:H7, *Campylobacter jejuni* and *Pseudomonas aeruginosa* under cold stress in low nutrient media. *Food Microbiol* 28:537–546. <https://doi.org/10.1016/j.fm.2010.11.002>
10. Passot S, Gautier J, Jamme F, Cenard S, Dumas P, Fonseca F (2015) Understanding the cryotolerance of lactic acid bacteria using combined synchrotron infrared and fluorescence microscopies. *The Analyst* 140:5920–5928. <https://doi.org/10.1039/C5AN00654F>
11. Saulou C, Jamme F, Girbal L, Maranges C, Fourquaux I, Cocaïgn-Bousquet M, Dumas P, Mercier-Bonin M (2013) Synchrotron FTIR microspectroscopy of *Escherichia coli* at single-cell scale under silver-induced stress conditions. *Anal Bioanal Chem* 405:2685–2697. <https://doi.org/10.1007/s00216-013-6725-4>
12. Gazi E, Dwyer J, Lockyer NP, Miyan J, Gardner P, Hart C, Brown M, Clarke NW (2005) Fixation protocols for subcellular imaging by synchrotron-based Fourier transform infrared microspectroscopy. *Biopolymers* 77:18–30. <https://doi.org/10.1002/bip.20167>
13. Lyng F, Gazi E, Gardner P (2011) Preparation of Tissues and Cells for Infrared and Raman Spectroscopy and Imaging. In: *Biomedical Applications of Synchrotron Infrared Microspectroscopy*, Royal Society of Chemistry. D. Moss, Dublin, pp 147–185
14. Vaccari L, Birarda G, Businaro L, Pacor S, Grenzi G (2013) Infrared Microspectroscopy of Live Cells in Microfluidic Devices (MD-IRMS): Toward a Powerful Label-Free Cell-Based Assay. *Analytical Chemistry* 84:4768–4775
15. Xie X, Zubarev RA (2014) Effects of Low-Level Deuterium Enrichment on Bacterial Growth. *PLoS ONE* 9:e102071. <https://doi.org/10.1371/journal.pone.0102071>

16. Holman H-YN, Miles R, Hao Z, Wozei E, Anderson LM, Yang H (2009) Real-Time Chemical Imaging of Bacterial Activity in Biofilms Using Open-Channel Microfluidics and Synchrotron FTIR Spectromicroscopy. *Anal Chem* 81:8564–8570. <https://doi.org/10.1021/ac9015424>
17. Tobin MJ, Puskar L, Barber RL, Harvey EC, Heraud P, Wood BR, Bambery KR, Dillon CT, Munro KL (2010) FTIR spectroscopy of single live cells in aqueous media by synchrotron IR microscopy using microfabricated sample holders. *Vib Spectrosc* 53:34–38. <https://doi.org/10.1016/j.vibspec.2010.02.005>
18. Vaccari L, Birada G, Greci G, Pacor S, Businaro L (2012) Synchrotron radiation infrared microspectroscopy of single living cells in microfluidic devices: advantages, disadvantages and future perspectives. *J Phys: Conf Ser* 359:012007. <https://doi.org/10.1088/1742-6596/359/1/012007>
19. Doherty J, Raouf A, Hussain A, Wolna M, Cinque G, Brown M, Gardner P, Denbigh J (2019) Live single cell analysis using synchrotron FTIR microspectroscopy: development of a simple dynamic flow system for prolonged sample viability. *Analyst* 144:997–1007. <https://doi.org/10.1039/C8AN01566J>
20. Chan KLA, Fale PLV, Atharawi A, Wehbe K, Cinque G (2018) Subcellular mapping of living cells via synchrotron microFTIR and ZnS hemispheres. *Anal Bioanal Chem* 410:6477–6487. <https://doi.org/10.1007/s00216-018-1245-x>
21. Chan KLA, Altharawi A, Fale P, Song CL, Kazarian SG, Cinque G, Untereiner V, Sockalingum GD (2020) Transmission Fourier Transform Infrared Spectroscopic Imaging, Mapping, and Synchrotron Scanning Microscopy with Zinc Sulfide Hemispheres on Living Mammalian Cells at Sub-Cellular Resolution. *Appl Spectrosc* 74:544–552. <https://doi.org/10.1177/0003702819898275>
22. Doherty J, Zhang Z, Wehbe K, Cinque G, Gardner P, Denbigh J (2018) Increased optical pathlength through aqueous media for the infrared microanalysis of live cells. *Anal Bioanal Chem* 410:5779–5789. <https://doi.org/10.1007/s00216-018-1188-2>
23. Marcotte L, Therien-Aubin H, Sandt C, Barbeau J, Lafleur M (2004) Solute Size Effects on the Diffusion in Biofilms of *Streptococcus mutans*. *Biofouling* 20:189–201. <https://doi.org/10.1080/08927010400010494>
24. Delille A, Quiles F, Humbert F (2007) In Situ Monitoring of the Nascent *Pseudomonas fluorescens* Biofilm Response to Variations in the Dissolved Organic Carbon Level in Low-Nutrient Water by Attenuated Total Reflectance-Fourier Transform Infrared Spectroscopy. *Appl Environ Microbiol* 73:5782–5788. <https://doi.org/10.1128/AEM.00838-07>
25. Comeau JWD, Pink J, Bezanson E, Douglas CD, Pink D, Smith-Palmer T (2009) A Comparison of *Pseudomonas Aeruginosa* Biofilm Development on ZnSe and TiO₂ Using Attenuated Total Reflection Fourier Transform Infrared Spectroscopy. *Appl Spectrosc* 63:1000–1007. <https://doi.org/10.1366/000370209789379259>
26. Quilès F, Humbert F, Delille A (2010) Analysis of changes in attenuated total reflection FTIR fingerprints of *Pseudomonas fluorescens* from planktonic state to nascent biofilm state. *Spectrochim Acta A* 75:610–616. <https://doi.org/10.1016/j.saa.2009.11.026>
27. Kuimova MK, Chan KLA, Kazarian SG (2009) Chemical Imaging of Live Cancer Cells in the Natural Aqueous Environment. *Appl Spectrosc* 63:164–171. <https://doi.org/10.1366/000370209787391969>
28. Kazarian SG, Chan KLA (2013) ATR-FTIR spectroscopic imaging: recent advances and applications to biological systems. *Analyst* 138:1940–1951. <https://doi.org/10.1039/C3AN36865C>
29. Meneghel J, Passot S, Dupont S, Fonseca F (2017) Biophysical characterization of the *Lactobacillus delbrueckii* subsp. *bulgaricus* membrane during cold and osmotic stress and its relevance for cryopreservation. *Appl Microbiol Biotechnol* 101:1427–1441. <https://doi.org/10.1007/s00253-016-7935-4>
30. Meneghel J, Passot S, Cenard S, Réfrégiers M, Jamme F, Fonseca F (2017) Subcellular membrane fluidity of *Lactobacillus delbrueckii* subsp. *bulgaricus* under cold and osmotic stress. *Appl Microbiol Biotechnol* 101:6907–6917. <https://doi.org/10.1007/s00253-017-8444-9>

31. Kong J, Yu S (2007) Fourier Transform Infrared Spectroscopic Analysis of Protein Secondary Structures. *Acta Biochim Biophys Sinica* 39:549–559. <https://doi.org/10.1111/j.1745-7270.2007.00320.x>
32. Delcour J, Ferain T, Deghorain M, Palumbo E, Hols P (1999) The biosynthesis and functionality of the cell-wall of lactic acid bacteria. *Antonie Van Leeuwenhoek International Journal of General and Molecular Microbiology* 76:159–184
33. Kleerebezem M, Hols P, Bernard E, Rolain T, Zhou M, Siezen RJ, Bron PA (2010) The extracellular biology of the lactobacilli. *FEMS Microbiology Reviews* 34:199–230. <https://doi.org/10.1111/j.1574-6976.2009.00208.x>
34. Chapot-Chartier M-P (2014) Interactions of the cell-wall glycopolymers of lactic acid bacteria with their bacteriophages. *Front Microbiol* 5:236. <https://doi.org/10.3389/fmicb.2014.00236>
35. Barth A (2007) Infrared spectroscopy of proteins. *Biochim Biophys Acta Bioenergetics* 1767:1073–1101. <https://doi.org/10.1016/j.bbabi.2007.06.004>
36. Yin X, Salemi MR, Phinney BS, Gotcheva V, Angelov A, Marco ML (2017) Proteomes of *Lactobacillus delbrueckii* subsp. *bulgaricus* LBB.B5 Incubated in Milk at Optimal and Low Temperatures. *mSystems* 2:e00027-17. <https://doi.org/10.1128/mSystems.00027-17>
37. De Angelis M, Calasso M, Cavallo N, Di Cagno R, Gobetti M (2016) Functional proteomics within the genus *Lactobacillus*. *Proteomics* 16:946–962. <https://doi.org/10.1002/pmic.201500117>
38. Streit F, Delettre J, Corrieu G, Béal C (2008) Acid adaptation of *Lactobacillus delbrueckii* subsp. *bulgaricus* induces physiological responses at membrane and cytosolic levels that improves cryotolerance. *J Appl Microbiol* 105:1071–1080. <https://doi.org/10.1111/j.1365-2672.2008.03848.x>
39. Serror P, Dervyn R, Ehrlich SD, Maguin E (2003) *csp*-like genes of *Lactobacillus delbrueckii* ssp. *bulgaricus* and their response to cold shock. *FEMS Microbiol Lett* 226:323–330. [https://doi.org/10.1016/S0378-1097\(03\)00594-9](https://doi.org/10.1016/S0378-1097(03)00594-9)
40. Schmid A, Kortmann H, Dittrich PS, Blank LM (2010) Chemical and biological single cell analysis. *Curr Opin Biotech* 21:12–20. <https://doi.org/10.1016/j.copbio.2010.01.007>
41. Wang D, Bodovitz S (2010) Single cell analysis: the new frontier in ‘omics.’ *Trends Biotechnol* 28:281–290. <https://doi.org/10.1016/j.tibtech.2010.03.002>
42. Lencastre Fernandes R, Nierychlo M, Lundin L, Pedersen AE, Puentes Tellez PE, Dutta A, Carlquist M, Bolic A, Schäpper D, Brunetti AC, Helmark S, Heins A-L, Jensen AD, Nopens I, Rottwitt K, Szita N, van Elsas JD, Nielsen PH, Martinussen J, Sørensen SJ, Lantz AE, Gernaey KV (2011) Experimental methods and modeling techniques for description of cell population heterogeneity. *Biotechnol Adv* 29:575–599. <https://doi.org/10.1016/j.biotechadv.2011.03.007>
43. Brehm-Stecher BF, Johnson EA (2004) Single-Cell Microbiology: Tools, Technologies, and Applications. *Microbiology and Molecular Biology Reviews* 68:538–559. <https://doi.org/10.1128/MMBR.68.3.538-559.2004>
44. Naumann D, Barnickel G, Bradaczek H, Labischinski H, Giesbrecht P (1982) Infrared Spectroscopy, a Tool for Probing Bacterial Peptidoglycan: Potentialities of Infrared Spectroscopy for Cell Wall Analytical Studies and Rejection of Models Based on Crystalline Chitin. *European Journal of Biochemistry* 125:505–515. <https://doi.org/10.1111/j.1432-1033.1982.tb06711.x>
45. Schuster KC, Urlaub E, Gapes JR (2000) Single-cell analysis of bacteria by Raman microscopy: spectral information on the chemical composition of cells and on the heterogeneity in a culture. *J Microbiol Methods* 42:29–38. [https://doi.org/10.1016/S0167-7012\(00\)00169-X](https://doi.org/10.1016/S0167-7012(00)00169-X)
46. Choo-Smith LP, Maquelin K, van Vreeswijk T, Bruining HA, Puppels GJ, Thi NAN, Kirschner C, Naumann D, Ami D, Villa AM, Orsini F, Doglia SM, Lamfarraj H, Sockalingum GD, Manfait M, Allouch P, Endtz HP

(2001) Investigating Microbial (Micro)colony Heterogeneity by Vibrational Spectroscopy. *Appl Environ Microbiol* 67:1461–1469. <https://doi.org/10.1128/aem.67.4.1461-1469.2001>

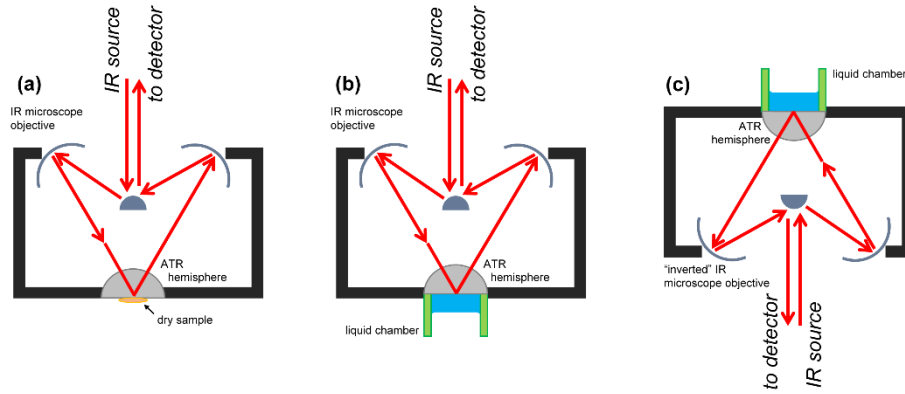


Fig.1 Schematic diagrams showing different Attenuated Total Reflectance-Fourier transform infrared (ATR-FTIR) microspectroscopy setups. **(a)** the setup described by Saulou *et al.* (2013) [11] and Passot *et al.* (2015) [10] for studying dried individual cells, **(b)** the setup described by Kuimova *et al.* (2009) [27] and Kazarian and Chan (2013) [28] for studying adherent live cells, and **(c)** the set up developed in this work for studying live non-adherent individual bacterial cells, the synchrotron radiation (SR)-based ATR-FTIR inverted microscope.

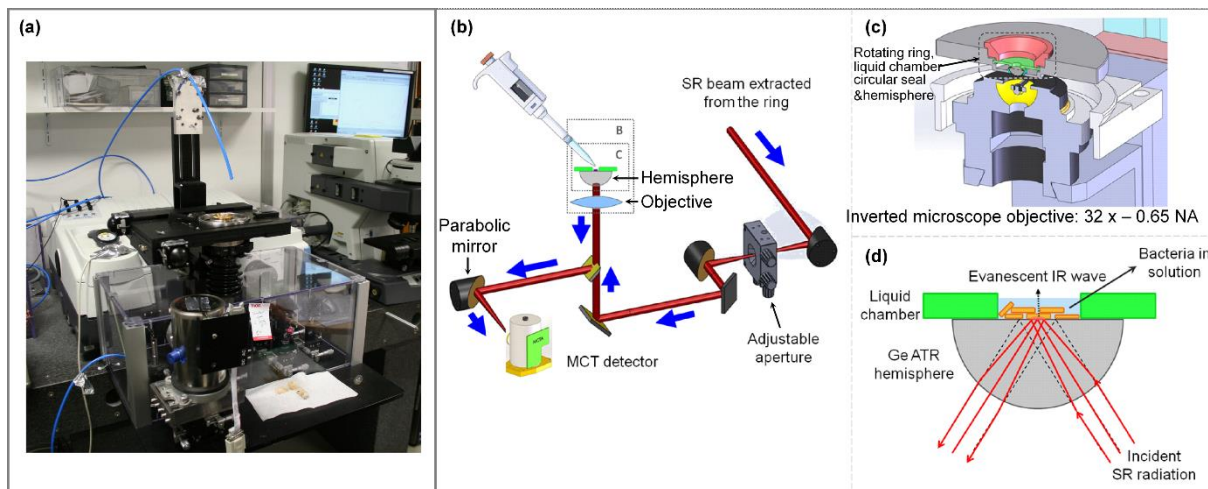


Fig.2 Picture **(a)** and diagrams **(b-d)** of the Attenuated Total Reflectance-Fourier transform infrared (ATR-FTIR) inverted microscope developed for the analysis of individual bacterial cells in an aqueous environment using synchrotron radiation (SR): **(b)** the overview of the optical path of the infrared beam, **(c)** a cross-section view of the microscope objective, hemisphere and liquid chamber, and **(d)** an enlargement diagram of the liquid sampling area showing the ATR principle.

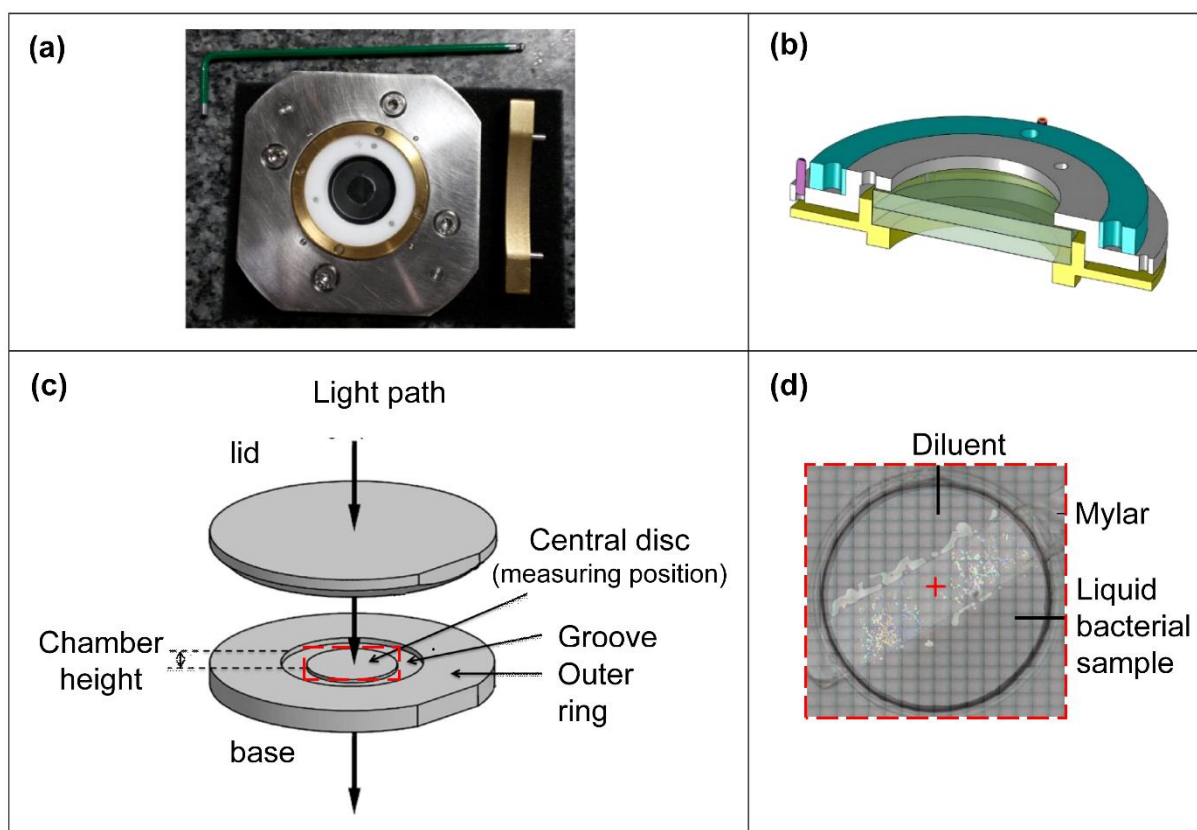


Fig.3 Prototype liquid sample device adapted to the motorized stage of the transmission FTIR microscope: **(a)** Picture of the home-made sample holder and tools used to mount and dismount the assembly, **(b)** technical drawing of the sample holder maintaining the micro-chamber tightly closed, **(c)** schematic view of a demountable CaF₂ micro-chamber, **(d)** mosaic image of the sampling area (enlargement of the red dotted area in **(c)**) where the diluent and liquid sample are separated by a thin strip of polyester film (Mylar®).

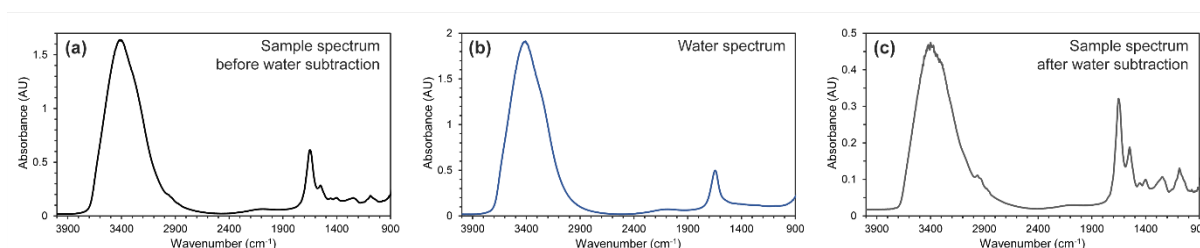


Fig.4 Illustration of the water subtraction procedure applied on pre-processed transmission infrared spectra, showing: **(a)** a sample spectrum recorded on a cluster of a few thousands of *L. bulgaricus* ATCC11842 cells in an aqueous environment, **(b)** a diluent (saline water) spectrum, and **(c)** the best result from the subtractions performed between the sample spectrum **(a)** minus the diluent spectrum **(b)** multiplied by the scaling factor 0.62 (further subtraction results with other scaling factors ranging from 0.6 to 1 are presented in Fig. S1).

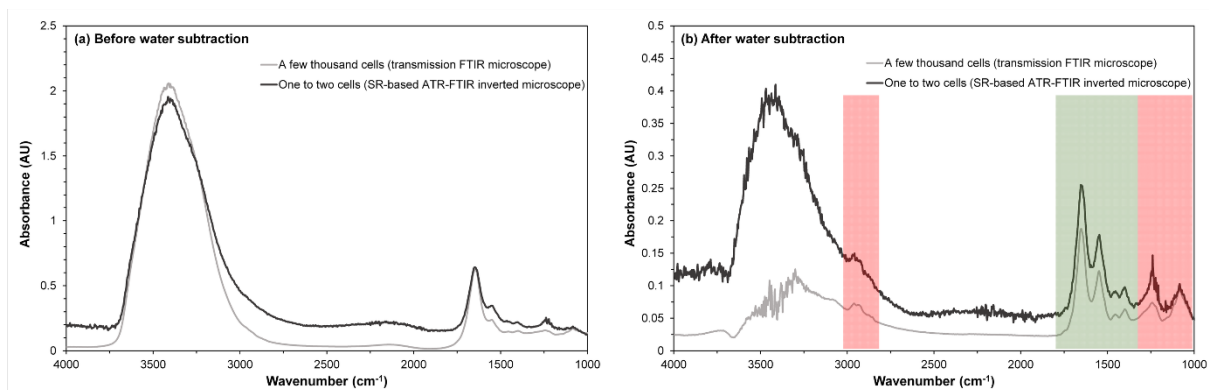


Fig.5 Example of pre-processed infrared spectra of live bacteria recorded with an SR-based ATR-FTIR inverted microscope (one to two cells) and thermal source-based FTIR transmission microscope (cluster of a few thousands of cells), before (a), and after (b) water subtraction. Green and red-coloured regions indicate the exploitable and non-exploitable spectral regions of spectra acquired at a single-cell level, respectively.

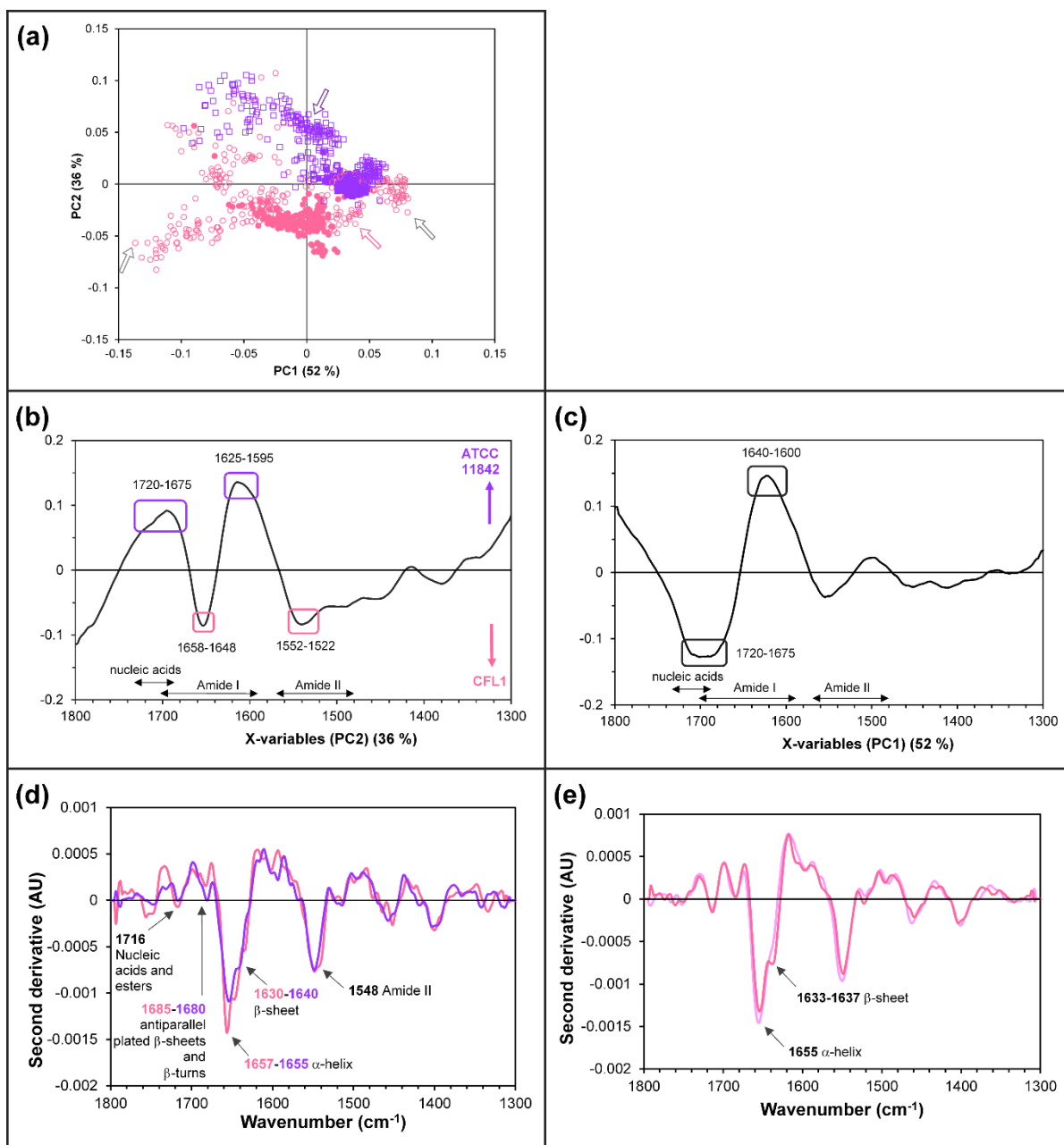


Fig.6 Principal Component Analysis (PCA) of processed FTIR spectra in the 1800 – 1300 cm⁻¹ region, of *L. bulgaricus* CFL1 bacteria (pink circles, freeze-sensitive) and *L. bulgaricus* ATCC 11842 bacteria (purple squares, freeze-resistant) acquired using the ATR-FTIR inverted microscope (open symbols, one to two cells) and using the transmission FTIR microscope (full symbols, clusters of a few thousands of cells) (a-c), and second derivatives (d-e) of selected points indicated by arrows in (a).

(a) Score plot of principal component 1 (PC1) vs. principal component 2 (PC2); (b) and (c): loading plots of the PC2 and PC1 axis, respectively. Positive peaks in PC2 characterized *L. bulgaricus* ATCC 11842 cells, whereas negative peaks characterized *L. bulgaricus* CFL1 cells, (d) second derivatives of two extreme points according to PC2 axis and obtained with the ATR-FTIR inverted microscope, corresponding to *L. bulgaricus* CFL1 (pink arrow in (a)) and *L. bulgaricus* ATCC 11842 (purple arrow in (a)), and (e) second derivatives of two extreme points according to PC1 axis and obtained with the ATR-FTIR inverted microscope, corresponding to *L. bulgaricus* CFL1 (grey arrows in (a)).

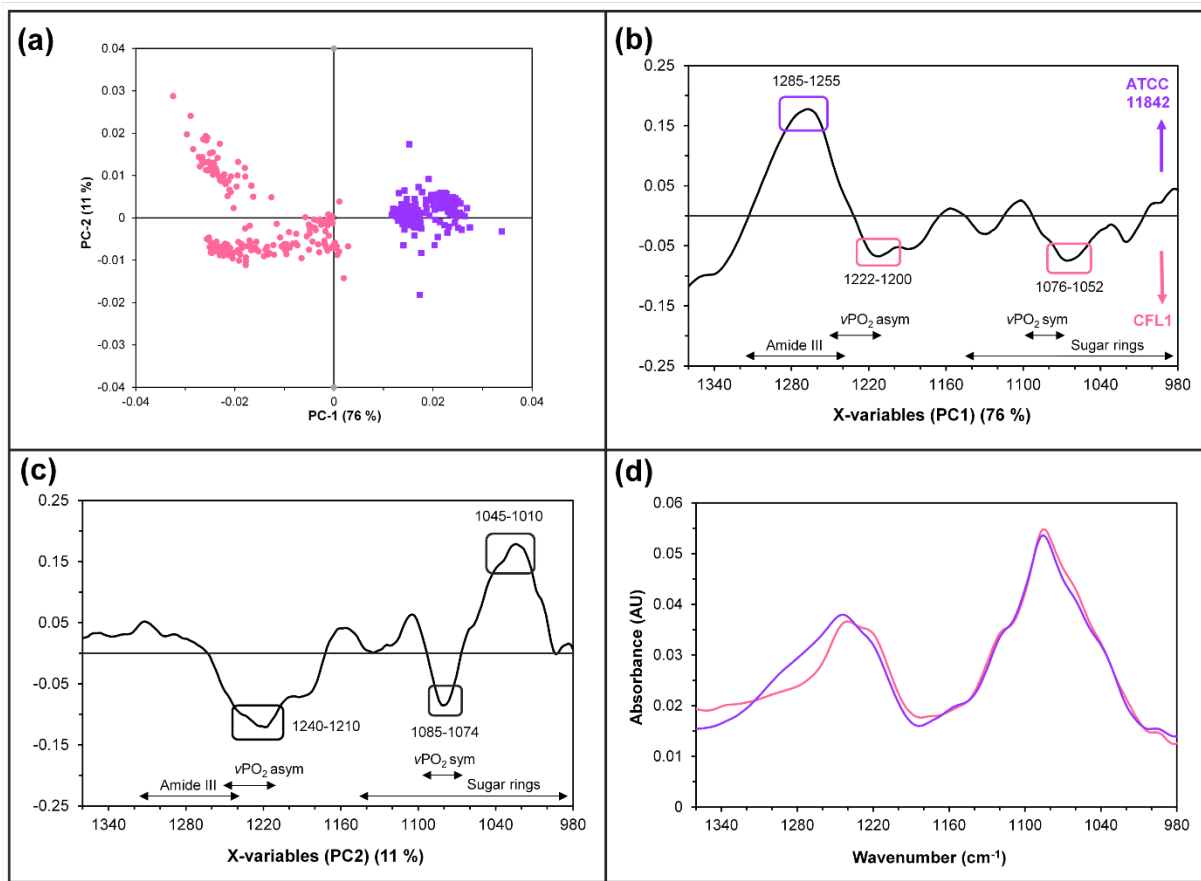


Fig.7 Principal Component Analysis (PCA) of processed FTIR spectra of *L. bulgaricus* CFL1 (pink circles, freeze-sensitive) and *L. bulgaricus* ATCC 11842 (purple squares, freeze-resistant) acquired using the transmission FTIR microscope (clusters of a few thousands of cells), in the 1360 – 975 cm⁻¹ region (a-c) and mean infrared spectra of *L. bulgaricus* ATCC 11842 (in purple) and *L. bulgaricus* CFL1 cells (in pink) (d).

(a) Score plot of principal component 1 (PC1) vs. principal component 2 (PC2), (b) and (c) loading plots of the PC1 and PC2 axis, respectively. Positive peaks in PC1 characterized *L. bulgaricus* ATCC 11842 cells, whereas negative peaks characterized *L. bulgaricus* CFL1 cells.

Analytical and Bioanalytical Chemistry

Electronic Supplementary Material

FTIR micro-spectroscopy using synchrotron-based and thermal source-based radiation for probing live bacteria

Julie Meneghel, Stephanie Passot, Frederic Jamme, Stephane Lefrançois, Pascale Lieben, Paul Dumas and Fernanda Fonseca

List of tables

Table S1. Assignments of main vibrational bands of the infrared spectra of <i>L. bulgaricus</i> in the 3000 – 975 cm ⁻¹ region, according to literature	3
Table S2. Comparison of information obtained with the two devices developed: a synchrotron radiation-based ATR-FTIR inverted microscope and a thermal-source transmission FTIR microscope	5

List of figures

Figure S1. Effect of the scaling factor values on the water subtraction procedure	6
Figure S2. Principal Component Analysis (PCA) of processed infrared spectra acquired using the synchrotron radiation-based ATR-FTIR inverted microscope, in the 1800 – 1300 cm ⁻¹ region	7
Figure S3. Principal Component Analysis (PCA) of processed infrared spectra acquired using the thermal-source transmission FTIR microscope, in the 1800 – 1300 cm ⁻¹ region.	8
Figure S4. Contribution of Principal Component 3 (PC3) to the Principal Component Analysis (PCA) presented in Fig. 6.	9
Figure S5. Second derivatives of extreme points selected from the PCA presented in Fig. 6, within the dataset acquired using the thermal-source transmission FTIR microscope	10
Figure S6. Contribution of Principal Component 3 (PC3) to the Principal Component Analysis (PCA) presented in Fig. 7	11

Table S1 Assignments of main infrared vibrational bands of the 3000 – 975 cm⁻¹ region of the infrared spectra of *L. bulgaricus*, according to literature.

Wavenumber range and ~ peak position (cm ⁻¹)		Assignment	Main biomolecule /cellular compounds/compartments associated	References
this work*	literature			
	~2961/2959/2956	$\nu_{as}-CH_3$		
	~2921/2925/2918	$\nu_{as} > CH_2$		
	~2875/2874/2872	ν_s-CH_3	Fatty acyl chain (membrane lipids)	[1–3]
	~2854/2852/2850	$\nu_s > CH_2$		
1720-1675	~1740/1736	$\nu C=O$	Esters from lipids / membranes	
	~1715/1713	$\nu C=O$	Esters, carboxylic acids	[1,2]
~1716/1713	1715-1680	$\nu C=O, \nu C=N, \nu C=C, \delta NH$	ADN/ARN bases /nucleic acids (weak features of nucleic acids often overlapped by amide I)	
	~1715/1713			
~1685-1680	1695-1662	Amide I ($\nu C=O$), antiparallel pleated β sheets and β -turns structures	Proteins (membranes, cytoplasm)	[1,4]
	~1695, 1685, 1675			
1658-1648	1657-1648	Amide I ($\nu C=O$),	Proteins (membranes, cytoplasm)	[1,4]
~1656, 1655	~1655, 1654	α -helical structures		
	~1645	random coiled structures		[3]
1640-1600 / 1625-1595	1641-1623	Amide I ($\nu C=O$),	Proteins (membranes, cytoplasm)	
~1640, 1637, 1633	~1637, 1633, 1624	antiparallel pleated β -sheet structures		
	~1585, 1570	νCOO^- asym	aspartate, glutamate	[1,3,4]
	~1516, 1518	$\nu CC, \delta CH$	tyrosine,	
	~1498, 1471	$\nu CCring$	phenylalanine	
1552-1522	1550 – 1520	amide II ($\delta N-H$ combined with $\nu C-N$)	Proteins (membranes, cytoplasm)	[1,5]
~1548	~1542/1540			
1468-1448	~1468/1470	C-H deformation /scissoring CH_2 ,	Proteins or fatty acyl chain (membrane lipids)	[1–3]
	~1455	C-H deformation /scissoring CH_3		
1420-1405	~1400	$\nu C=O$ sym of COO^-	Amino acids, fatty acyl chains (peptidoglycan)	[2,3]
	~1415	$\nu C-O$ sym of COO^-	In phospholipids only	[3]
1285-1255	1310-1240	Amide III ($\nu C-N$ combined with $\delta N-H$)	Proteins (membranes, cytoplasm)	[1,3]
	~1250			
1222-1200	1250-1220	νPO_2^- asym	Phosphodiester, phospholipids (membrane),	
1240-1210	~1243/1238		teichoic acids, lipoteichoic acids (cell wall),	
	~1218		nucleic acids (nucleoid)	[1,2,6,7]
1076-1052	1200 – 900	$\nu C-O, \nu C-C,$	Polysaccharides, sugar rings (cell wall,	
1045-1010	~1060, 1040, 1150, 1100	C-O-C deformation, $\nu P-O-C, \nu P-O-P$	peptidoglycan)	
1085-1074	1095 – 1075	νPO_2^- sym	Phosphodiester, phospholipids (membrane),	
	~1085		nucleic acids (nucleoid)	[1,7]

(ν : stretching, δ : bending, sym.: symmetric, asym.: antisymmetric); * ~peak positions obtained from the second derivatives of spectra presented in Figure 6 and Fig.S5.

References Table S1

1. Naumann D. Infrared Spectroscopy in Microbiology. Encyclopedia of Analytical Chemistry. John Wiley & Sons, Ltd; 2006.
2. Quilès F, Humbert F, Delille A. Analysis of changes in attenuated total reflection FTIR fingerprints of *Pseudomonas fluorescens* from planktonic state to nascent biofilm state. Spectrochim Acta A [Internet]. 2010 [cited 2020 Mar 16];75:610–6. Available from: <https://linkinghub.elsevier.com/retrieve/pii/S1386142509006027>
3. Le Gal J-. M, Manfait M, Theophanides T. Applications of FTIR spectroscopy in structural studies of cells and bacteria. J Mol Struct. 1991;242:397–407.
4. Barth A. Infrared spectroscopy of proteins. Biochim Biophys Acta Bioenergetics [Internet]. 2007 [cited 2015 Feb 4];1767:1073–101. Available from: <http://linkinghub.elsevier.com/retrieve/pii/S0005272807001375>
5. Filip Z, Herrmann S, Kubat J. FT-IR spectroscopic characteristics of differently cultivated *Bacillus subtilis*. Microbiol Res [Internet]. 2004 [cited 2020 Mar 16];159:257–62. Available from: <https://linkinghub.elsevier.com/retrieve/pii/S0944501304000473>
6. Naumann D, Barnickel G, Bradaczek H, Labischinski H, Giesbrecht P. Infrared Spectroscopy, a Tool for Probing Bacterial Peptidoglycan: Potentialities of Infrared Spectroscopy for Cell Wall Analytical Studies and Rejection of Models Based on Crystalline Chitin. European Journal of Biochemistry [Internet]. 1982 [cited 2020 Mar 16];125:505–15. Available from: <http://doi.wiley.com/10.1111/j.1432-1033.1982.tb06711.x>
7. Movasaghi Z, Rehman S, Rehman I. Fourier Transform Infrared (FTIR) Spectroscopy of Biological Tissues. Appl Spectrosc Rev [Internet]. 2008 [cited 2015 Feb 4];43:134–79. Available from: <http://www.tandfonline.com/doi/abs/10.1080/05704920701829043>

Table S2 Comparison of information obtained with the two devices developed: a synchrotron radiation-based ATR-FTIR inverted microscope and a thermal-source transmission FTIR microscope.

PCA combining data sets of ATR-FTIR inverted microscope and FTIR transmission microscope				
	PC1	Heterogeneity within bacterial populations	Amide I, Nucleic acids	
	PC2	Sub-populations of bacterial strains ATCC 11842: PC2 positive direction, CFL1: PC2 negative direction,	Amide I, Amide II, Nucleic acids	
	PC3	Sub-populations of bacterial strains Heterogeneity within CFL1 population ATCC 11842: PC3 negative direction CFL1: PC3 negative and positive direction	Amide I, Amide II, Nucleic acids	
PCA with data sets of ATR-FTIR inverted microscope				
	PC1	Heterogeneity within bacterial populations	Amide I, Nucleic acids	
	PC2	Sub-populations of bacterial strains ATCC 11842: PC2 positive direction, CFL1: PC2 negative direction	Amide I, Amide II, Nucleic acids	
	PC3	Sub-populations of bacterial strains Heterogeneity within CFL1 population ATCC 11842: PC3 negative direction CFL1: PC3 negative and positive direction	Amide I, Amide II, Nucleic acids, Lipids or proteins (1468-1448 cm ⁻¹)	
PCA with FTIR transmission microscope				
	PC1	Bacterial strains ATCC 11842: PC1 positive direction CFL1: PC1 negative direction	Amide I, Amide II, Nucleic acids	
	PC2	Heterogeneity within CFL1 population	Amide I, Amide II, Nucleic acids	
	PC3	Heterogeneity within CFL1 population	Amide II	
Main infrared vibrational bands characterizing each strain and the heterogeneity within bacterial population*				
		ATR-FTIR inverted microscope and FTIR transmission microscope	ATR-FTIR inverted microscope	FTIR transmission microscope
	CFL1	1716-1700, 1658-1648, 1555-1522, 1420-1405	1716-1700, 1658-1648, 1555- 1522, 1468-1448, 1420-1405	1715-1695, 1658-1650, 1552-1522, 1468-1448
	ATCC	1720-1675, 1670-1660, 1625-1595, 1420-1405	1720-1675, 1670-1660, 1625- 1595, 1420-1405	1625-1595
	Heterogeneity	1720-1675, 1640-1600	1720-1675, 1640-1600	1700-1675, 1645-1630

* obtained from the loading plots of each corresponding PCA (either performed on the combined data set comprising the data obtained with the ATR-FTIR inverted microscope and the transmission FTIR microscope, or on the data set of each device separately)

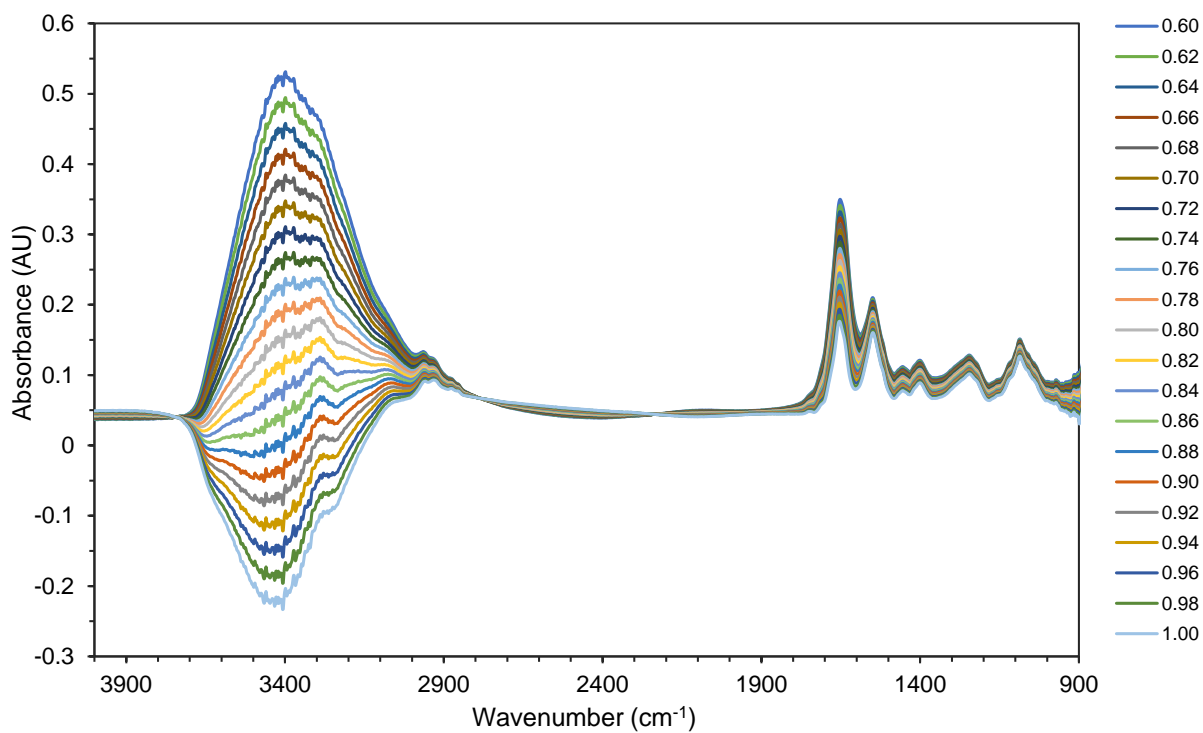


Fig. S1 Effect of the scaling factor values on the water subtraction procedure. Example of a set of spectra obtained after the subtraction of the diluent spectrum (Fig. 4b) to the pre-processed sample spectrum (Fig. 4a) for different scaling factors (from 0.6 to 1 with a step of 0.02).

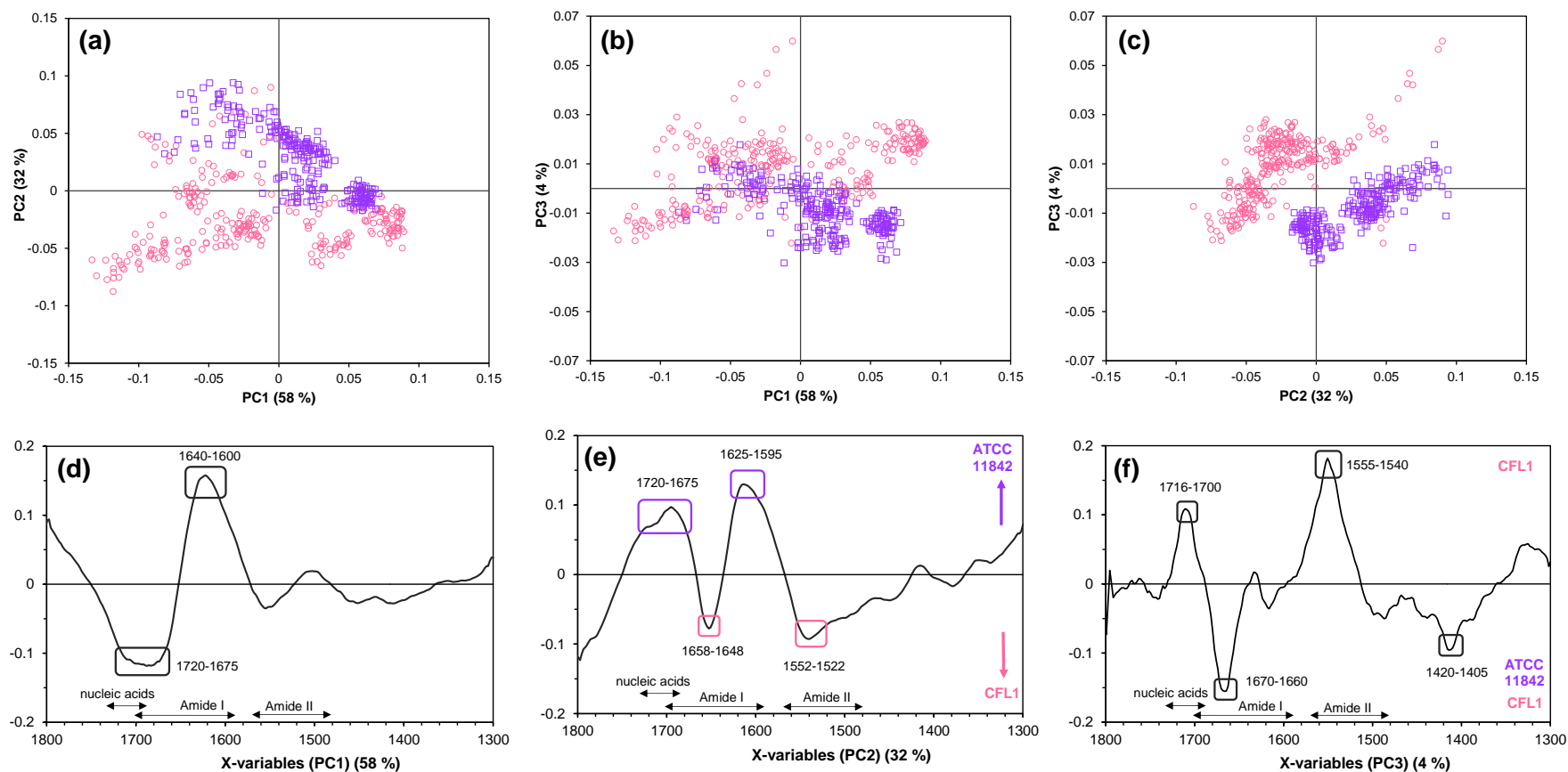


Fig. S2 Principal Component Analysis (PCA) of processed infrared spectra acquired using the synchrotron radiation-based ATR-FTIR inverted microscope (one to two cells), in the 1800 – 1300 cm^{-1} region. (a), (b) and (c) Score plots of principal component 2 (PC2) vs. principal component 1 (PC1), PC3 vs PC1 and PC3 vs PC2, respectively. (d), (e) and (f) loading plots of the PC1, PC2 and PC3 axes, respectively. Positive peaks in PC2 characterized *L. bulgaricus* ATCC 11842 cells, whereas negative peaks characterized *L. bulgaricus* CFL1 cells. Positive peaks in PC3 characterized *L. bulgaricus* CFL1 cells, whereas negative peaks mainly characterized *L. bulgaricus* ATCC 11842 cells and a sub-population of *L. bulgaricus* CFL1 cells.

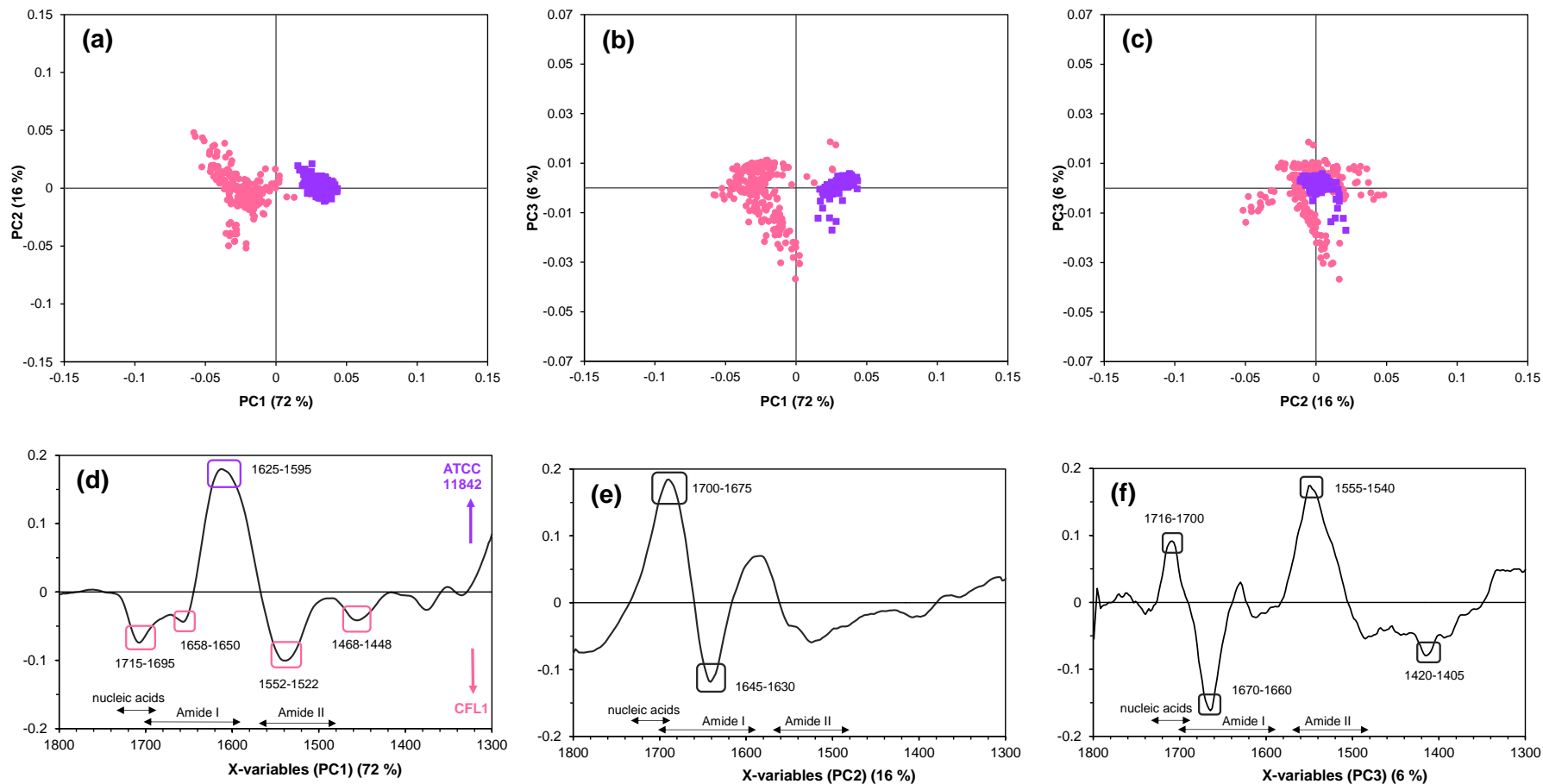


Fig. S3 Principal Component Analysis (PCA) of processed infrared spectra acquired using the thermal-source transmission FTIR microscope (a few thousands of cells), in the 1800 – 1300 cm^{-1} region. (a), (b) and (c) Score plots of principal component 2 (PC2) vs. principal component 1 (PC1), PC3 vs PC1 and PC3 vs PC2, respectively. (d), (e) and (f) loading plots of the PC1, PC2 and PC3 axis, respectively. Positive peaks in PC1 characterize *L. bulgaricus* ATCC 11842 cells (freeze-resistant), whereas negative peaks characterize *L. bulgaricus* CFL1 cells. PC2 and PC3 loading plots display main spectral variations within both bacterial populations.

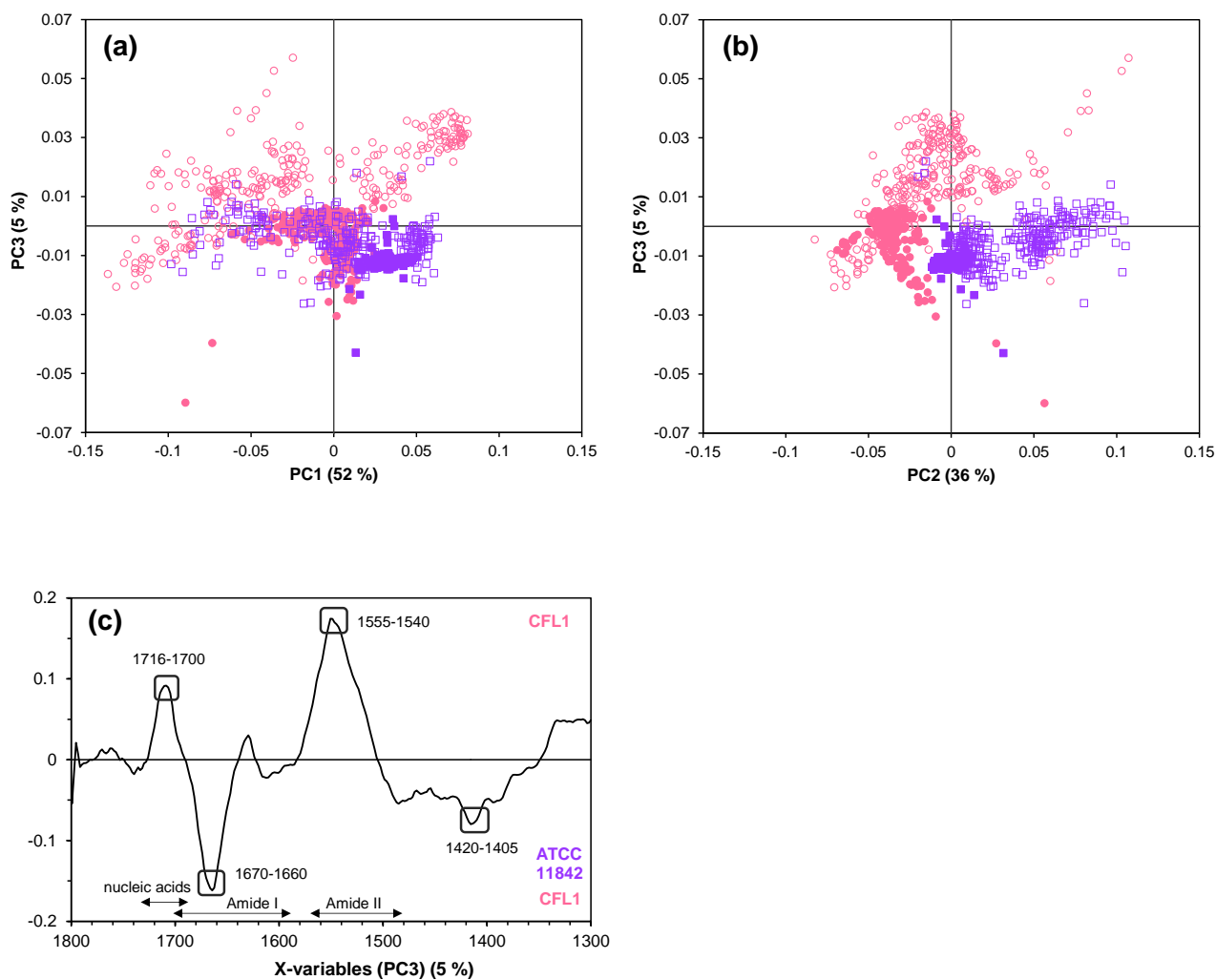


Fig. S4 Contribution of Principal Component 3 (PC3) to the Principal Component Analysis (PCA) of processed infrared spectra in the 1800 – 1300 cm^{-1} region (Fig. 6), of *L. bulgaricus* CFL1 bacteria (pink circles, freeze-sensitive) and *L. bulgaricus* ATCC 11842 bacteria (purple squares, freeze-resistant) acquired using the ATR-FTIR inverted microscope (open symbols, one to two cells) and using the transmission FTIR microscope (full symbols, clusters of few thousands of cells). (a) and (b) Score plots of principal component 3 (PC3) vs. principal component 1 (PC1) and PC3 vs. PC2, respectively. (c) Loading plot of the PC3 axis. Positive peaks in PC3 characterized *L. bulgaricus* CFL1 cells, whereas negative peaks mainly characterized *L. bulgaricus* ATCC 11842 cells and a subpopulation of *L. bulgaricus* CFL1 cells.

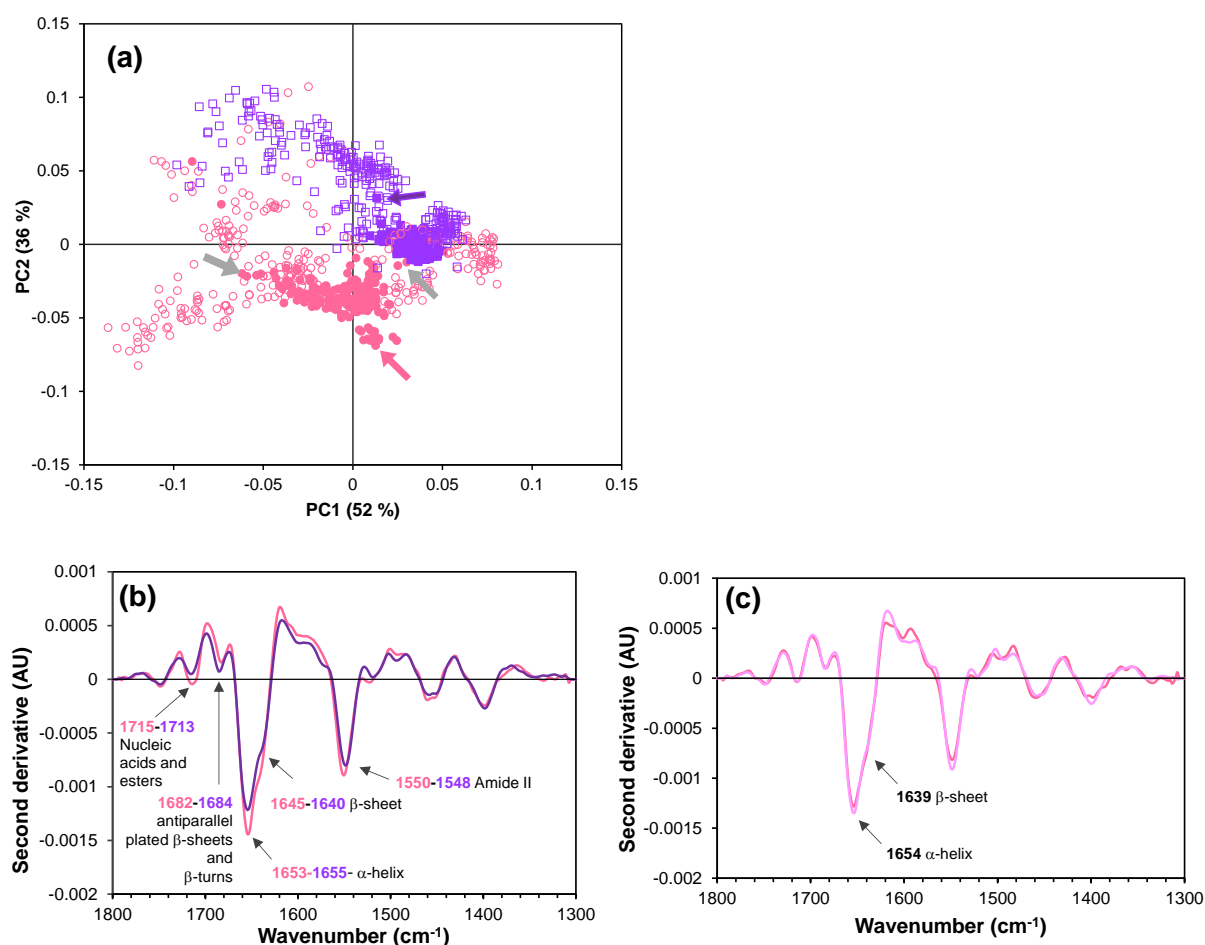


Fig. S5 Second derivatives of extreme points selected from the PCA presented in Fig. 6, within the dataset acquired using the thermal-source transmission FTIR microscope.

(a) Score plot of Principal component 2 (PC2) vs PC1 from Principal Component Analysis (PCA) of processed infrared spectra in the 1800 – 1300 cm^{-1} region, of *L. bulgaricus* CFL1 bacteria (pink circles, freeze-sensitive) and *L. bulgaricus* ATCC 11842 bacteria (purple squares, freeze-resistant) acquired using the ATR-FTIR inverted microscope (open symbols, one to two cells) and using the transmission FTIR microscope (full symbols, clusters of few thousands of cells) in the 1800-1300 cm^{-1} region, (Fig. 6a). Arrows indicate the extreme points selected to calculate the second derivatives; (b) second derivatives of two extreme points (spectra) according to PC2, corresponding to *L. bulgaricus* CFL1 (pink arrow in (a)) and *L. bulgaricus* ATCC 11842 (purple arrow in (a)), (c) second derivatives (Savitsky-Golay algorithm; 9 points, 3rd order) of two extreme points according to PC1, corresponding to *L. bulgaricus* CFL1 (grey arrows in (a)).

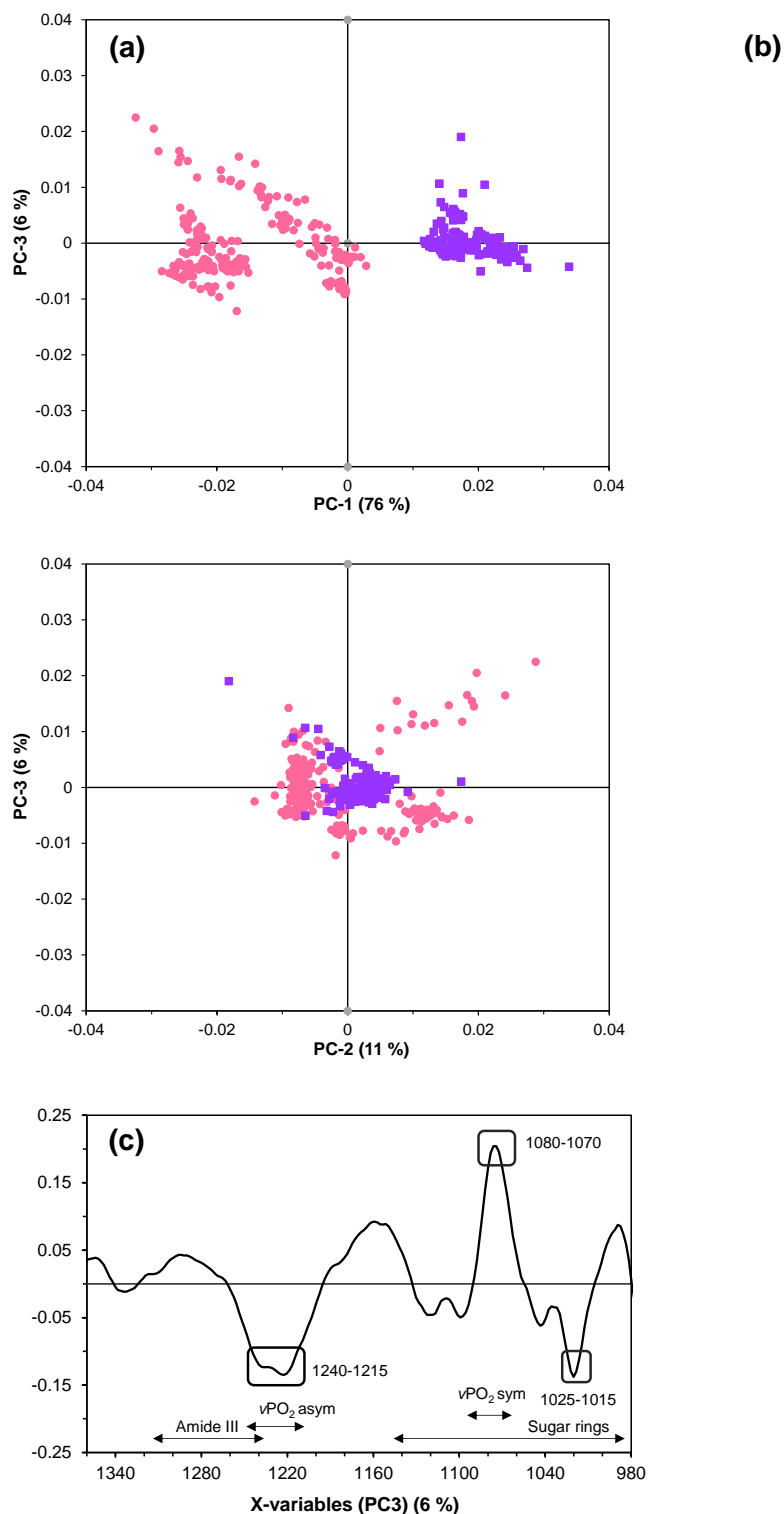


Fig. S6 Contribution of Principal Component 3 (PC3) to the Principal Component Analysis (PCA) of processed infrared spectra of *L. bulgaricus* CFL1 (pink circles, freeze-sensitive) and *L. bulgaricus* ATCC 11842 (purple squares, freeze-resistant) acquired using the transmission FTIR microscope (clusters of few thousands of cells) (Fig. 7), in the 1360 – 975 cm^{-1} region. (a) and (b) Score plots of principal component 3 (PC3) vs. principal component 1 (PC1) and PC3 vs PC2, respectively. (c) Loading plot of the PC3 axis.